

# The Persistence of Memory in Ionic Conduction Probed by Nonlinear Optics

Andrey D. Poletayev<sup>1,2,\*</sup>, Matthias C. Hoffmann<sup>3</sup>, James A. Dawson<sup>4,5</sup>, Samuel W. Teitelbaum<sup>1,6,7</sup>, Mariano Trigo<sup>1,6</sup>, M. Saiful Islam<sup>8</sup>, Aaron M. Lindenberg<sup>1,2,6,\*</sup>

## Abstract

**The rates of many temperature-activated transport processes, such as ionic diffusion in battery electrolytes, follow the Arrhenius relation. Predicting the practical rates and activation energies from atomistic descriptors enables the rational design of materials, devices, and processes. However, this is complicated by the often correlated mechanisms of transport<sup>1-3</sup>, and by ambiguity even in the vibrational origin of translation, called the attempt frequency for ionic hopping<sup>4,5</sup>. Here we show that single-cycle terahertz pumps impulsively trigger the fundamental step of diffusion, ionic hopping, in battery solid electrolytes. This is visualized by an induced transient birefringence enabling direct probing of ionic hopping on the picosecond timescale. We show further that the relaxation of the transient signal measures the temporal decay of memory, and the production of entropy in diffusion. We extend experimental results with *in silico* transient birefringence to identify attempt frequencies for ion hopping. Our results demonstrate the potential of non-linear optical methods to probe the mechanisms of non-equilibrium transport phenomena.**

## Introduction

Mass transport processes, such as thermally activated ionic diffusion in the solid state, are critical to energy technology. In the framework of transition state theory<sup>6,7</sup>, ionic diffusion is a random walk composed of fundamental steps between lattice sites, called hops. Hops are considered rare events originating randomly with an attempt frequency  $\nu_0$ , and succeeding with a probability determined by the Gibbs free energy of the transition state<sup>8,9</sup>, considered the energy barrier between two stable states at lattice sites. However, the atomistic vibrational nature of the attempt frequency remains under debate<sup>3-5</sup>. Even more importantly, between the macroscopic and the vibrational regimes, transport dynamics are non-Markovian and sub-diffusive due in part to the exchange of internal states and the presence of memory<sup>10-13</sup>. This affects both the timing and directionality of hops<sup>12</sup>: an ion's walk is not random at timescales shorter than the decay of the memory kernel for diffusion. In the framework of a generalized master equation<sup>13,14</sup>, a nonzero memory kernel implies the need to know a system's history to determine subsequent dynamics. It is characterized by fourth-moment or Burnett-order statistics<sup>12,13</sup>, and determines the dispersion of AC conductivity between the picosecond and the macroscopic timescales<sup>11,12</sup>. The development

---

<sup>1</sup> Stanford Institute for Materials and Energy Sciences, SLAC National Laboratory, Menlo Park, CA, USA

<sup>2</sup> Department of Materials Science and Engineering, Stanford University, Stanford, CA, USA

<sup>3</sup> Linac Coherent Light Source, SLAC National Accelerator Laboratory, Menlo Park, CA, USA

<sup>4</sup> Chemistry – School of Natural and Environmental Sciences, Newcastle University, Newcastle upon Tyne, UK

<sup>5</sup> Centre for Energy, Newcastle University, Newcastle upon Tyne, UK

<sup>6</sup> Stanford PULSE Institute, SLAC National Accelerator Laboratory, Menlo Park, CA 94025, USA

<sup>7</sup> Present Address: Department of Physics, Arizona State University, Tempe, AZ 85287, USA

<sup>8</sup> Department of Chemistry, University of Bath, Bath, UK

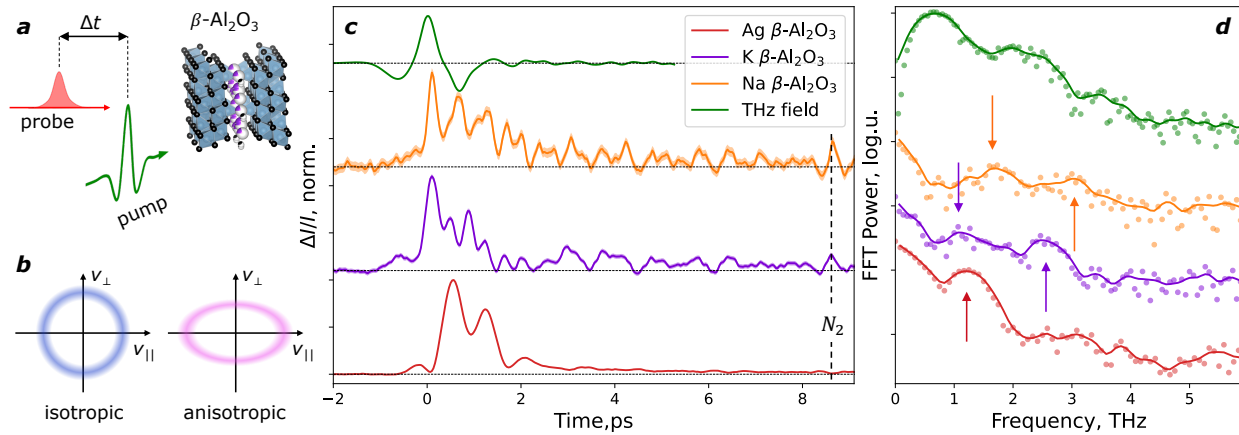
\* Correspondence to [andrey.poletayev@gmail.com](mailto:andrey.poletayev@gmail.com), [aaronl@stanford.edu](mailto:aaronl@stanford.edu).

of mechanistic models of transport incorporating path-dependent non-equilibrium dynamics<sup>15</sup> hinges on the characterization of memory in transport. Like for chemical reactions, the timescale to initiate an ionic hop ( $1/\nu_0$ ) may be short, with  $\nu_0$  typically in the terahertz range, but the timescale of memory may be orders of magnitude longer. Yet, this timescale has not been measured experimentally, due in part to the insensitivity of static or steady-state probes to memory effects.

## Results and Discussion

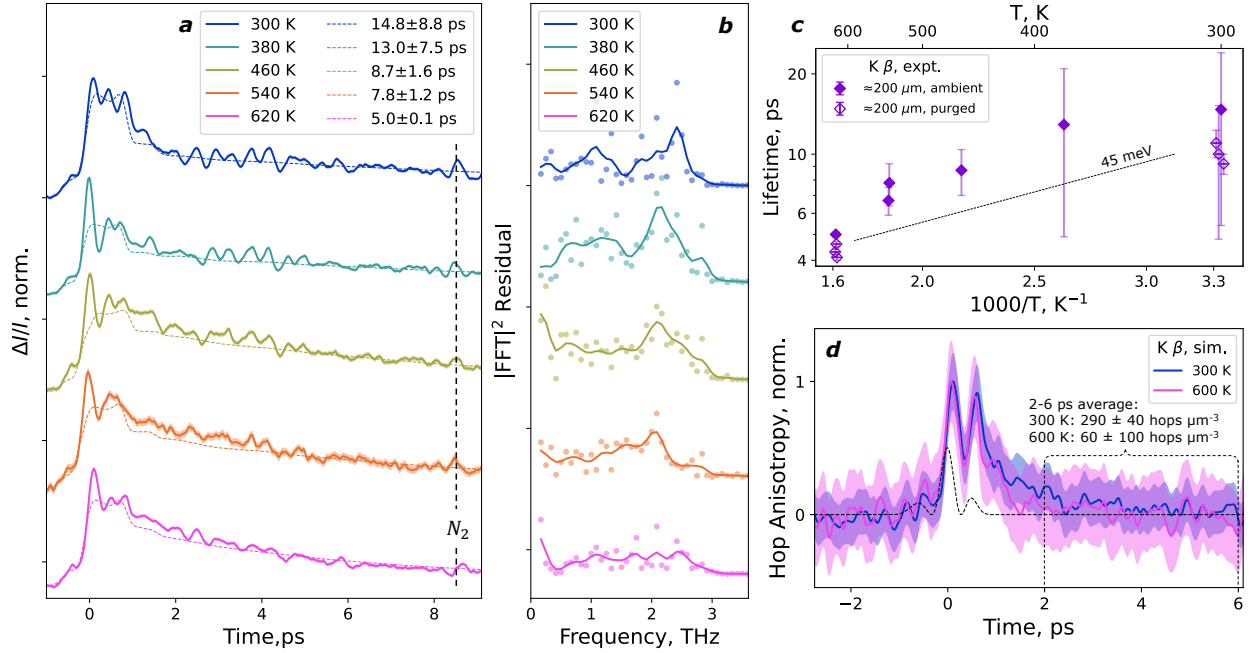
A measurement of memory effects requires the ability to repeatedly and impulsively excite hopping events<sup>16</sup>. Furthermore, a probe of non-equilibrium ion transport must match the timescale of  $\nu_0$  and be sensitive to ionic vibrations<sup>17,18</sup> and anisotropy<sup>19,20</sup>. Conceptually, ultrafast optical  $\chi^{(3)}$ -based methods offer an opportunity to match nonlinear hydrodynamics giving rise to the memory kernel<sup>12,13</sup>. However, past pump-probe studies of lattice dynamics have focused on small-amplitude coherent oscillatory displacements of bound vibrational modes<sup>21–24</sup>. Here we show that rare, stochastic, and large-amplitude translations such as ion hops ( $\approx 3.3$  Å in  $\beta$ -aluminas), the fundamental steps of solid-state mass transport and conductivity, are also accessible. We probe the ionic response of model fast ionic conductors  $\beta$ -aluminas ( $M_{1+2x}Al_{11}O_{17+x}$ , where the mobile ion  $M^+ = Na^+, K^+, Ag^+$ , and  $x \approx 0.1$ ) following an impulsive excitation with single-cycle terahertz pulses. The pulses are generated by optical rectification in lithium niobate<sup>25,26</sup> with a center frequency  $\approx 0.7$  THz, and with the pump field  $E \perp c$  axis of the crystals and parallel to the conduction plane (Figure 1a). In  $\beta$ -aluminas, the extensively characterized<sup>27–33</sup> vibrational modes of the mobile ions within the conduction planes occur at 0.7–3.0 THz. The transient birefringence of the sample is probed via stimulated Raman scattering of a second, time-delayed pulse (terahertz Kerr effect, TKE) in transmission. Because the TKE signal arises from an emitted electric field, it represents the time derivative of the polarization within the sample<sup>34,35</sup>, and in the absence of electron transfer is proportional to ionic velocities<sup>21</sup>. For the unperturbed isotropic distribution of ion velocities, all emitted fields cancel, yielding zero signal. Only an anisotropic distribution of ion velocities produces a net signal (Figure 1b).

Figure 1c shows the time traces of the terahertz-pumped transient birefringence of the three  $\beta$ -aluminas at 300K, along with the temporal profile of the pump pulse. All samples show both oscillatory and non-oscillatory responses at 300K as well as at 620K (Extended Data Figure 1). Such incoherent, non-oscillatory relaxation has been previously observed in liquids<sup>36–38</sup> and solids<sup>17,39</sup>, and attributed to overdamped rotational or librational modes. However, there are no such rotational modes in  $\beta$ -aluminas. While the magnitude of the birefringence response scales with the square of the pump field (Figure S3), we do not observe any spectral changes with increasing pump fluence in either birefringence or transmission experiments (Figures S3, S5), and the liquid-like relaxation is substantially slower than the vibrational components. Therefore, we also rule out nonlinear phonon coupling<sup>23,24</sup>. Otherwise, the vibrational components of the TKE signal (Figure 1d) are consistent with established spectroscopic signatures of mobile ions in  $\beta$ -aluminas.



**Figure 1 | Terahertz Kerr effect (TKE) in  $\beta$ -alumina ion conductors.** (a) Schematic of the transient birefringence experiment: terahertz pump (green) perturbs mobile ions (purple) in the ionic conductor, and transmission of the 800 nm probe pulse (pink) delayed by a time  $\Delta t$  yields a transient birefringence. (b) Origination of a transient birefringence signal. With an isotropic distribution of ion velocities (left), the emitted fields parallel and perpendicular to the pump cancel. An anisotropic distribution of ion velocities (right) produces net ellipticity in the emitted signal field. (c) Time-domain traces of transient birefringence in  $\beta$ -alumina ion conductors:  $\text{Na}^+$  (orange),  $\text{K}^+$  (purple),  $\text{Ag}^+$  (dark red), and electro-optic sampling trace of the pump field (green). The shaded regions correspond to  $\pm 1$  s.e. of the mean signal at each time delay. The labeled feature at 8.4 ps is the rotational coherence of atmospheric nitrogen<sup>40</sup> within a Rayleigh length ( $> 500 \mu\text{m}$ ) of the samples ( $\leq 30 \mu\text{m}$  thick). (d) Fourier transform power spectra (points) of the signals in (c), and smoothed with a Gaussian filter of 0.1 THz st. dev. (lines), with peaks highlighted by arrows.

We investigate the possible connection between temperature-activated hopping conduction and the picosecond TKE relaxation by varying the temperature of the samples. In all materials, the signals from thinner ( $< 30 \mu\text{m}$ ) vs thicker ( $100\text{--}300 \mu\text{m}$ ) samples match after the short-time oscillations dephase (Extended Data Figure 2), and subsequent non-oscillatory relaxation represents a bulk material response. This relaxation is absent in the non-resonant optical Kerr response (Extended Data Figure 6). We use thicker samples to enhance the long-time non-oscillatory signal, and model it using a sum of a response arising from intrinsic nonlinearity and a mismatch in optical constants between the pump and probe frequencies<sup>41,42</sup> (which scales with the sample thickness and is eliminated for thin samples, as in Figure 1c), and single-exponential decay, shown as dashed lines (Figure 2a, and Extended Data Figures 3-5). The residuals of this TKE fit (Figure 2b) show the same frequency,  $\approx 2$  THz, as the optical Kerr response (Extended Data Figure 6), suggesting that both pumps excite coherent ionic vibrations, but the terahertz pump excites an additional response that decays incoherently. For K  $\beta$ -alumina, the non-oscillatory relaxation following the THz pump accelerates from  $\approx 10$  ps at 300 K to  $\approx 4$  ps at 620 K (Figure 2ac). For measurements done in ambient atmosphere, the time constants are slightly slower due to the overlaid signal from atmospheric water vapor<sup>19</sup>, which is slower than the sample response (Figure S1). For Ag and Na  $\beta$ -aluminas, the TKE relaxation times were faster, and the temperature dependences weaker, than for K  $\beta$ -alumina.



**Figure 2 | Temperature dependence of the long-lived TKE in  $K^+$   $\beta$ -alumina.** (a) Time-domain traces of transient birefringence in  $K^+$   $\beta$ -alumina in ambient atmosphere (solid lines), normalized and offset for clarity. The shaded regions correspond to  $\pm 1$  s.e. of the mean signal. Colored dashed lines are fits to the sum of single-exponent relaxation and an instantaneous polarization. The labeled feature at 8.4 picoseconds is the rotational coherence of atmospheric nitrogen. (b) Fourier transform power spectra (points) of the residuals of fitting the signals in (a) to single exponentials and instantaneous polarization components and smoothed with a Gaussian filter of 0.1 THz standard deviation (lines). (c) Time constants of single-exponential fits to the long-lived TKE component in ambient atmosphere (filled symbols) and dry atmosphere (empty symbols). Error bars are  $\pm 1$  s.e. The dashed line representing an activation energy of 45 meV is a guide to the eye. (d) Normalized simulated anisotropy of hopping directions under applied electric field mimicking the lithium niobate terahertz pump at 300 K (blue) and 600 K (pink). Black dashed line: square of the simulated electric field. The shaded area is the s.e. of the mean signal at each simulated temperature.

Having eliminated all other possible mechanisms, we propose that the liquid-like picosecond-timescale component of the TKE response arises from the activated incoherent hopping of mobile ions driven by the pump pulse. We use large-scale molecular dynamics simulations with an applied pulsed electrical field<sup>19,43,44</sup> mimicking the experimental THz pump to verify this hypothesis. Following the simulated pump pulse, the times and directions of all hopping events in the simulation are recorded, and their anisotropy is calculated (Figure 2c). While hopping events are rare and uncertainties relatively large, a simulation with 800 iterations of  $\approx 5000$  mobile ions each yields a statistically significant difference in the hopping anisotropy at 2-6 ps after the peak applied field (Figure 2c) between 300 K and 600 K. The simulated anisotropy of hopping, triggered by the simulated laboratory-strength pump pulse, exhibits a picosecond-timescale relaxation that decays faster at 600 K than at

300 K, in agreement with experiment. We conclude that the picosecond-timescale TKE response in  $\beta$ -aluminas is a signature of pump-triggered anisotropic hopping of mobile ions.

We now focus on the mechanism for the relaxation of this signal. TKE measures not an isotropic enhancement in the hopping rate, but the *preference* of hopping along or against the pump. Yet, the TKE measurement does not distinguish velocities parallel to the pump from those anti-parallel to it ( $+v_{\parallel}$  versus  $-v_{\parallel}$  in Figure 1b). Similarly, hopping rates both parallel and antiparallel to the field contribute to the signal. In the TKE experiment, following impulsive pump-triggered hops along the applied field, the mobile ions preferentially hop back after some time, and this preference for back-hops corresponds to the temperature-activated non-oscillatory relaxation in TKE. Therefore, TKE provides an experimental measurement of the orientational part of memory in ionic diffusion, which favors the opposite-direction back-hop at short timescales<sup>11,12</sup>. The activation energy for it is  $\approx 40$ -50 meV (Figure 2b), much lower than the low-frequency activation energy ( $>200$  meV)<sup>45</sup> of the ionic conductivity in K  $\beta$ -alumina, but similar to that of high-frequency NMR relaxation,  $\approx 50$ -60 meV<sup>46</sup>. The faster and more weakly activated TKE relaxation in Na and Ag  $\beta$ -aluminas is consistent with faster overall transport and smaller expected high-frequency activation energies than in K  $\beta$ -alumina (Supplementary Note 4). Given that NMR does not rely on triggering ionic hops at all, and yields similar activation to TKE, we rule out selective probing of a subset of transport events as the difference between the activation energies from picosecond TKE and low-frequency conductivity. TKE does not selectively probe a subset of low-activation ion motions but highlights the dominant process at picosecond timescales: correlated back-hopping. This is consistent with steady-state simulations: the fastest hops are the most strongly correlated, while the slowest hops are the most random<sup>12</sup>. The increase in activation energies measured from the picosecond to the macroscopic timescales<sup>47</sup> arises at least in part from the slow randomization of hopping and loss of memory, that is, from the slow production of entropy.

All three  $\beta$ -aluminas show a picosecond “tail” in the TKE response, and in all of them the memory kernel is expected to persist for longer than the timescale of measurable TKE response<sup>12</sup>. To further verify the memory in ionic transport as the origin of the “tail” in TKE, we seek a system where memory loss is fast, i.e., ion transport proceeds via a true random walk even at the picosecond timescale, and the “tail” can be expected to vanish rapidly. By contrast with  $\beta$ -aluminas, in the TKE response of  $K^+$   $\beta''$ -alumina ( $K_{1.67}Al_{10.67}Li_{0.33}O_{17}$ ), we observe a long-lived relaxation at 300 K, but not at 620 K (Figure 3a). The simulated anisotropy of hopping following a 0.7 THz pump exhibits a long-lived relaxation at 300 K, but not at 600 K (Figure 3c), in agreement with experiment. At 2-4 ps following the terahertz pump, the simulated anisotropy of hopping is statistically distinct from zero at 300 K, but not at 600 K. This is consistent with a long-time memory at 300 K, and its fast decay, i.e. a true random walk, at 620 K<sup>12</sup>. The quantitative discrepancy between the relative strength of the long-lived component between simulation and experiment may be due in part to spectral dependence of front-surface reflection, which is assumed  $\approx 50\%$  and spectrally independent. We conclude that the incoherent picosecond-timescale relaxation of the terahertz Kerr effect indeed corresponds to the presence of memory in ionic hopping at these timescales.

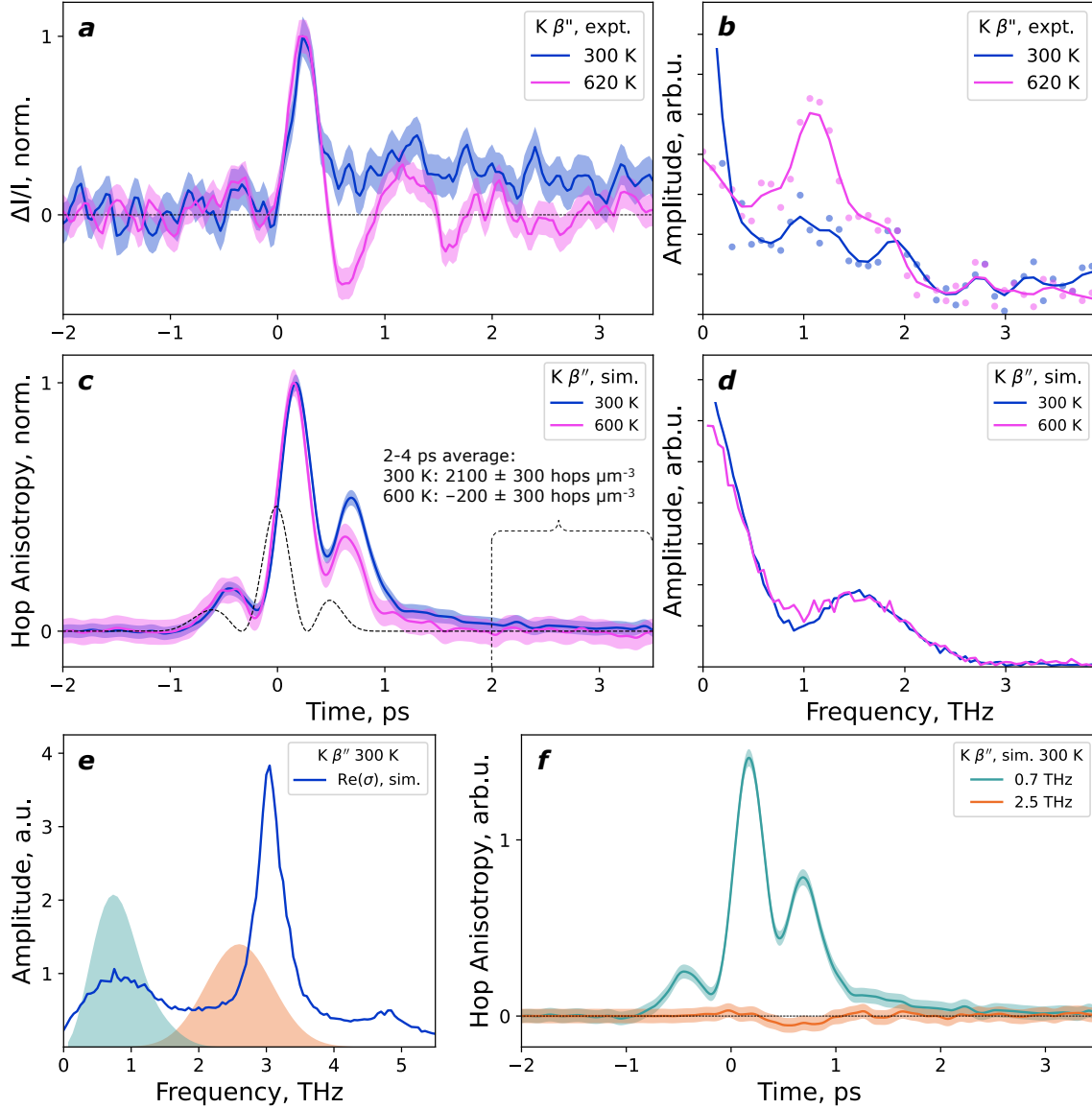


**Figure 3 | Terahertz Kerr effect in  $K^+ \beta''$ -alumina.** (a) Normalized time-domain traces of transient birefringence in thin polycrystalline  $K^+ \beta''$ -alumina at 300 K (blue) and 620 K (pink). The shaded regions are  $\pm 1$  s.e. of the mean signals. (b) Fourier transform amplitude spectra of the signals in (a). (c) Normalized simulated anisotropy of hopping directions in polycrystalline  $K^+ \beta''$ -alumina under applied electric field mimicking the lithium niobate terahertz pump at 300 K (blue) and 600 K (pink). Black dashed line: square of the simulated electric field. The shaded area is  $\pm 1$  s.e. of the mean signals. (d) Fourier transform amplitude spectra of the signals in (c). (e) Simulated 2D in-plane optical  $K^+$  conductivity of  $K^+ \beta''$ -alumina in the terahertz region (blue). Peaks at 1, 3, and  $\approx 5$  THz are in agreement with experiment<sup>48</sup>. Shaded: spectra of simulated applied electric fields with center frequencies 0.7 THz (teal) mimicking the experimental lithium niobate pump (a) and simulated in (c), and 2.5 THz (orange). (f) Simulated anisotropy of hopping directions in polycrystalline  $K^+ \beta''$ -alumina at 300 K under applied electric fields centered at 0.7 THz, same as in (c), and 2.5 THz (orange). Shaded areas:  $\pm 1$  s.e. of the mean signals.

To cause an anisotropy in hopping, the pump field (experimental or simulated) must directly couple to the vibrational modes from which hopping originates, i.e., the attempt frequencies, and trigger hopping aligned with the polarization of the applied field. This must happen before thermalization, or else pump-driven heating enhances all hopping rates isotropically (Figure 1b). Having established the correspondence of the experimental TKE and simulated anisotropy of ionic hopping, we use additional *in silico* TKE at pump frequencies presently inaccessible to us experimentally to identify attempt frequencies for ionic hopping. We simulate the anisotropy of hopping in  $K^+ \beta''$ -alumina following a pump pulse centered at 2.5 THz that overlaps with the strong infrared-active vibration of the  $K^+$  ions in the conduction plane at 3.0 THz (Figure 3ef, orange). Despite the material absorbing nearly the same amount of energy from simulated pulses at 0.7 THz and 2.5 THz of equal peak fields (Figure S6), and despite the 3.0 THz vibration being coherently driven by the 2.5 THz pulse (Figure S7), the 0.7 THz pulse creates a  $\sim 20\times$  stronger anisotropy of hopping than the 2.5 THz pulse (Figure 3f). This suggests that the pulse at  $\sim 1$  THz couples directly to hops, whereas the 2.5 THz pulse heats the material isotropically. We conclude that the attempt frequency in  $K^+ \beta''$ -alumina is  $\sim 1$  THz. The excitation of this vibration is evident in the experimental TKE response (Figure 3ab). The attempt frequencies in  $\beta$ -aluminas can be identified similarly from simulation once the dynamics of bound defect clusters and non-equivalent lattice sites are considered (Supplementary Note 5).

## Conclusions

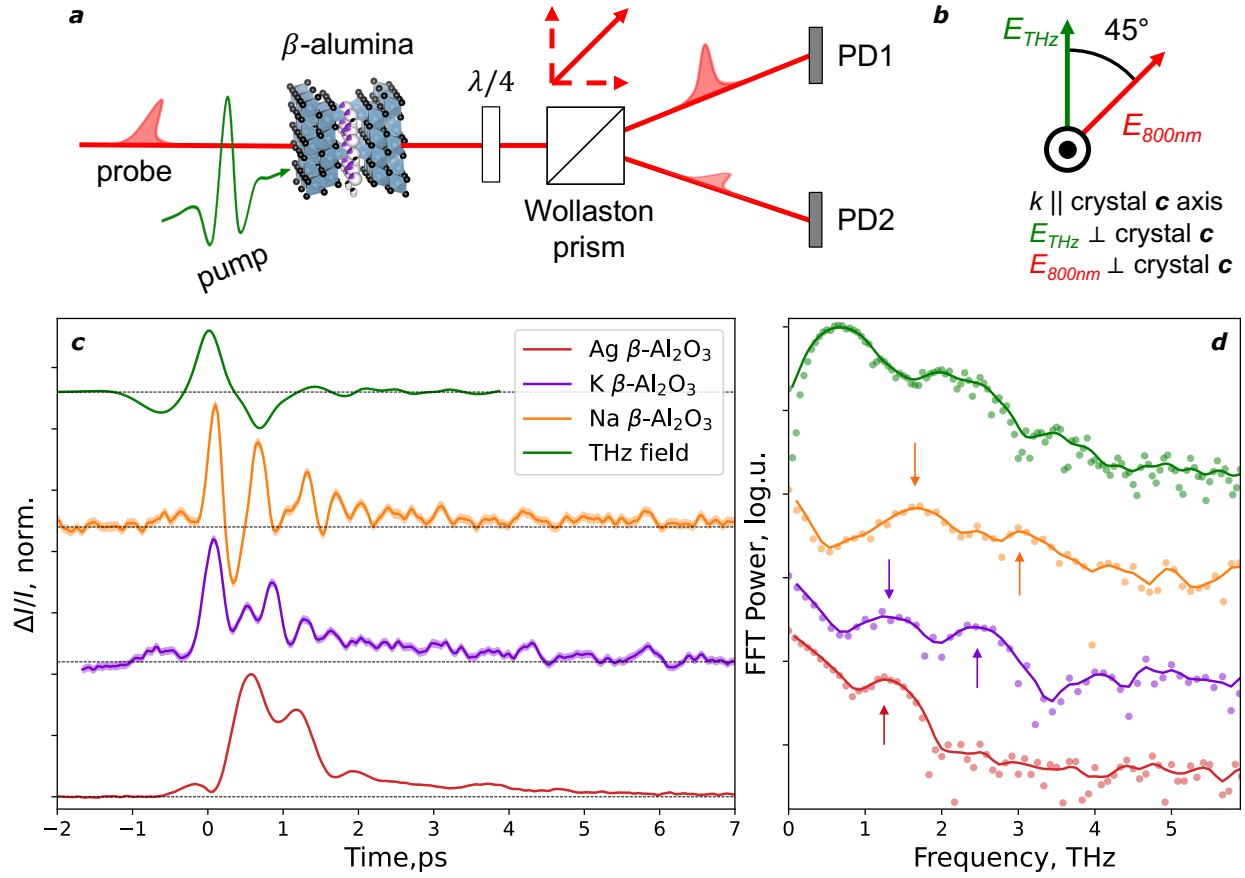
In summary, we have used impulsive resonant terahertz excitation to trigger ionic hopping. Picosecond relaxation of the terahertz Kerr effect arises from back-hopping within a multi-hop mechanism of transport. This effect is absent if the excitation is non-resonant, or if ion diffusion proceeds via a true random walk. Therefore we establish TKE, a nonlinear optical measurement, as a direct probe of memory in transport<sup>12,13</sup>. TKE highlights both the origination of ionic conduction, i.e., the attempt frequency, and the entropy production during the slow loss of memory of an initial site in diffusion. Beside probing the mechanisms of ionic conduction, the nonlinear effects we highlight gain significance for transport under strong driving forces, at short timescales, and in confined dimensions. We expect these findings to advance understanding of the nonequilibrium thermodynamics of transport and the accurate parameterization of coarse-grained and multiscale models of transport, such as Monte-Carlo and phase-field models. This knowledge can be applied to accelerate progress in electrochemical energy conversion, heterogeneous catalysis, nanofluidics, engineering phase transformations, and neuromorphic computing.

## Acknowledgements

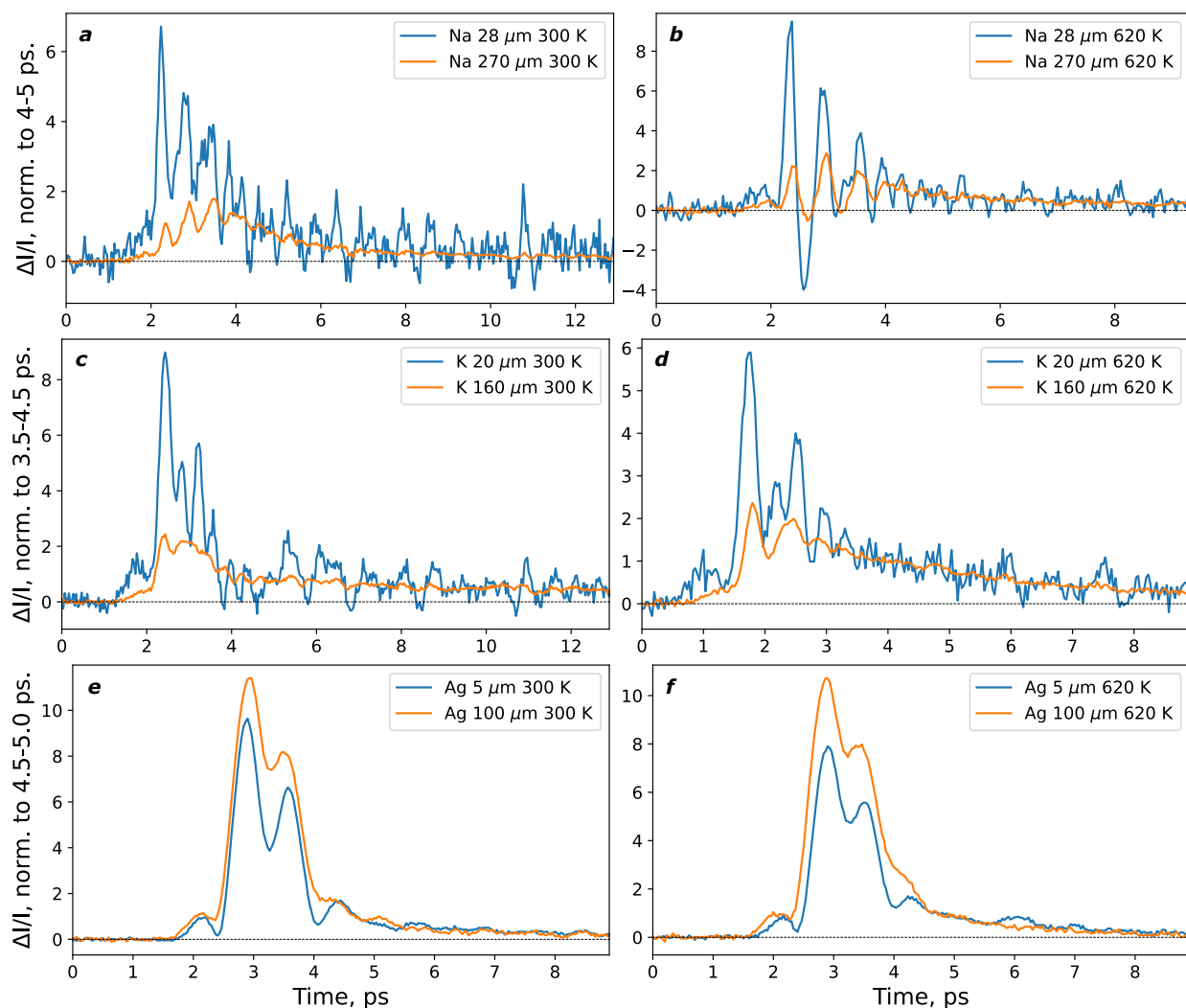
This work was supported by the U.S. Department of Energy, Office of Basic Energy Sciences, Division of Materials Sciences and Engineering (contract DE-AC02-76SF00515). MSI and JAD gratefully acknowledge the EPSRC Programme Grant “Enabling next generation lithium batteries” (EP/M009521/1). JAD gratefully acknowledges the EPSRC (EP/V013130/1), Research England (Newcastle University Centre for Energy QR Strategic Priorities Fund) and Newcastle University (Newcastle Academic Track (NUAcT) Fellowship) for funding. We are indebted to Prof. Osamu Kamishima for sharing single crystals of Na  $\beta$ -alumina with us.

### Author Contributions

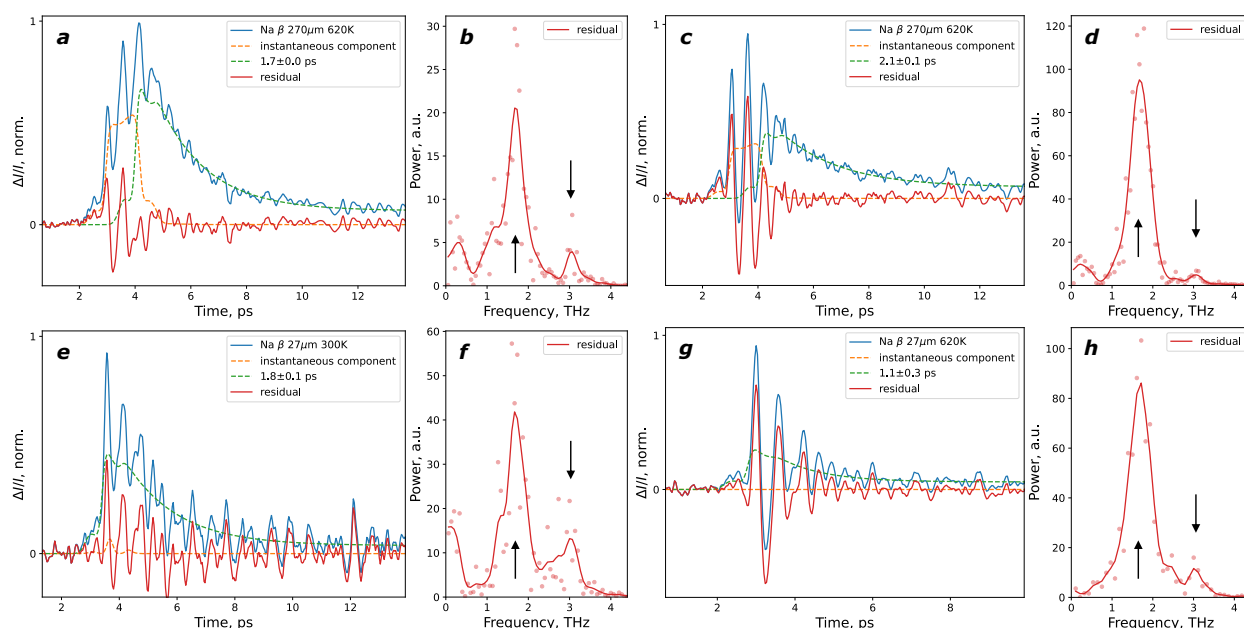
The probing of ionic transport with nonlinear techniques was proposed by AML, MT, SWT, and ADP. Simulations incorporating the terahertz pump were proposed by AML, JAD, and MSI. ADP and MCH performed the terahertz Kerr effect and transmission measurements. ADP, SWT, and MT performed the optical Kerr effect measurements. ADP analyzed the experimental data. ADP performed and analyzed the molecular dynamics simulations with advice from JAD and MSI. AML advised and supervised the work. All authors contributed to the writing of the manuscript.



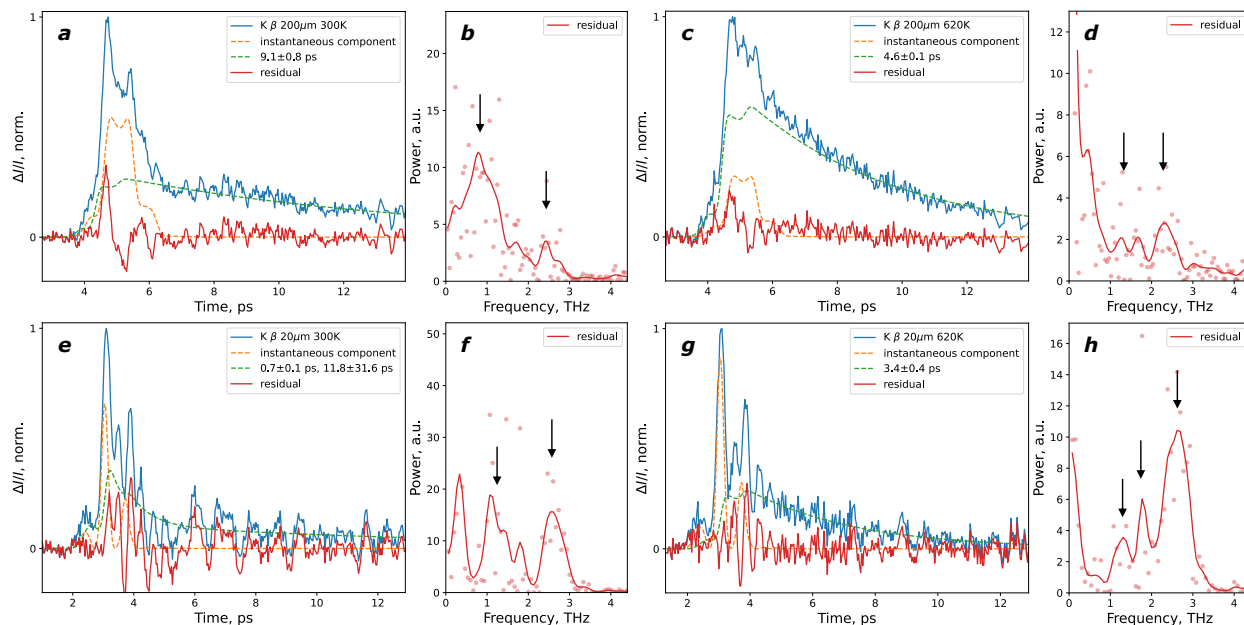
**Extended Data Figure 1 | Terahertz Kerr effect (TKE) in  $\beta$ -aluminas at elevated temperature.** (a) Schematic of the transient birefringence experiment: terahertz pump (green) perturbs mobile ions (purple) in the ionic conductor. The 800 nm probe pulse (pink) delayed by a time  $\Delta t$  is split with a quarter wave plate and a Wollaston prism. The polarization rotation of the probe pulse is detected with a pair of Si photodiodes in a balanced detection scheme. (b) Polarizations of the pump and probe pulses relative to each other and the  $\beta$ -alumina crystals. (c) Time-domain traces of transient birefringence in thin single crystals of  $\beta$ -aluminas at 620 K:  $\text{Na}^+$  (orange),  $\text{K}^+$  (purple),  $\text{Ag}^+$  (dark red), and electro-optic sampling trace of the pump field (green). The shaded regions correspond to  $\pm 1$  s.e. of the mean signal at each time delay. (d) Fourier transform power spectra (points) of the signals in (c), and smoothed with a Gaussian filter of 0.1 THz st. dev. (lines), with peaks highlighted by arrows.



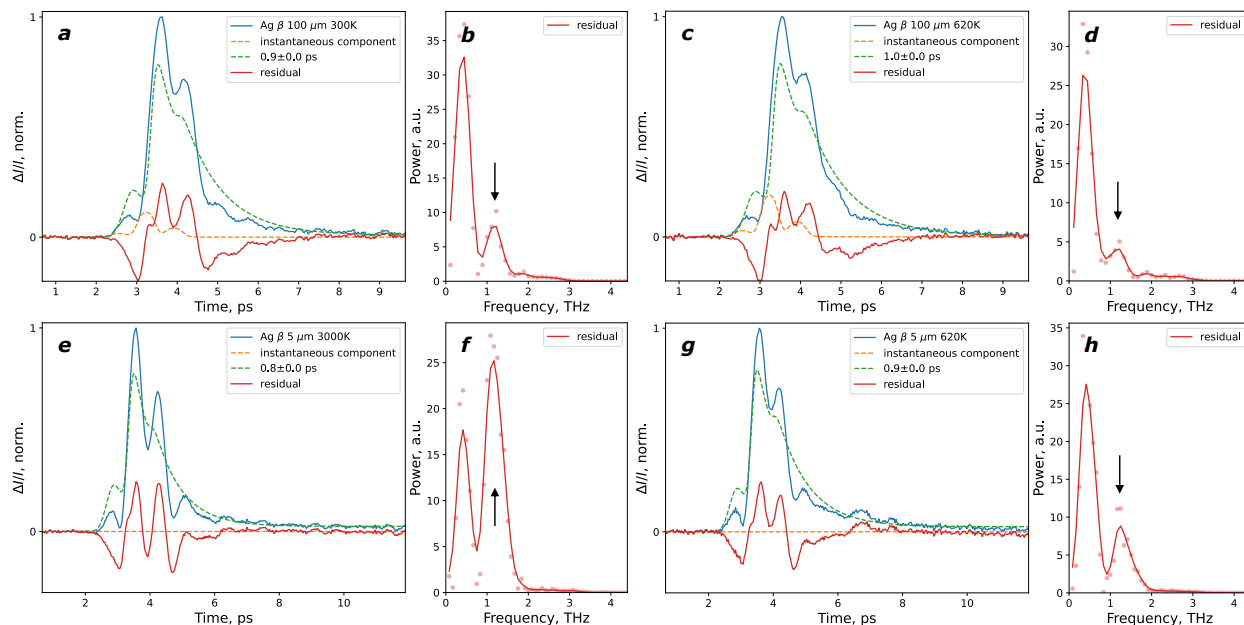
**Extended Data Figure 2 | TKE in  $\beta$ -aluminas with varying sample thickness.** TKE signals for thick ( $\geq 100 \mu\text{m}$ ) and thin ( $\leq 30 \mu\text{m}$ ) crystals of Na (**ab**), K (**cd**), and Ag (**ef**)  $\beta$ -alumina, normalized to their values at a pump-probe delay time when short-time oscillatory signal components have decayed. For all materials at 300 K (**ace**) and 620 K (**bdf**) the longer-time relaxation of the signals overlap. Since the TKE signal is phase accumulated over the sample thickness, thicker samples yield lower-noise signals at long time delays.



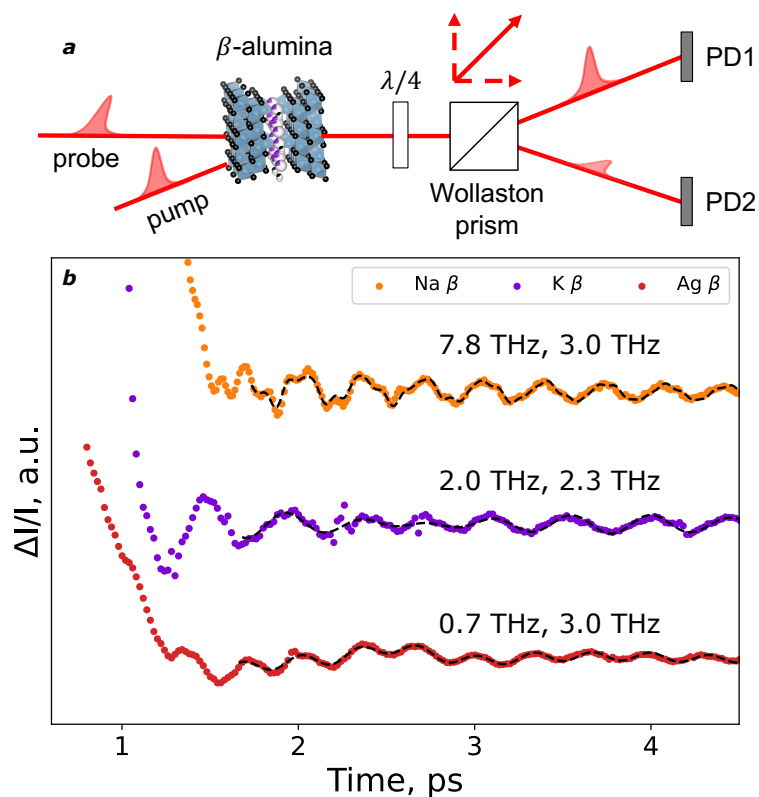
**Extended Data Figure 3 | Fitting TKE signals of Na  $\beta$ -alumina.** Each signal (blue in **a-c-g**) was measured in a purged atmosphere and modeled as the sum of an instantaneous component (orange) and a single-exponential relaxation (green) with a long-time constant (Supplementary Notes 1 and 2). For the thin sample (**e-h**), the strength of the instantaneous component was small. The strong vibrational component in the thick-sample signal (**a-d**) precluded unambiguous fitting at short times, so the exponential component was fit to the long-time part of the signal. The residuals (dark red) are oscillatory. Their Fourier transforms (**b-d-f-h**), plotted with 0.1-THz Gaussian-filter smoothing, show main frequency components at 1.8 and 3.0 THz in agreement with non-resonant OKE (3.0 THz, Extended Data Figure 6), literature, and simulation (1.7 THz, Figure S7).



**Extended Data Figure 4 | Fitting TKE signals of K  $\beta$ -alumina.** Each signal (blue in **a**-**g**) was measured in a purged atmosphere and modeled as the sum of an instantaneous component (orange) and a single-exponential relaxation (green) with a long-time constant (Supplementary Notes 1 and 2). For the thin sample (**e**-**h**), the instantaneous component was non-negligible, and at 300 K a weakly determined second exponential was identifiable. The residuals (dark red) are oscillatory and most interpretable in the signals from the thin sample (**e**-**h**). Their Fourier transforms (**b**, **d**, **f**, **h**), plotted with 0.1-THz Gaussian-filter smoothing, show main frequency components at  $\approx 1.2$ ,  $\approx 2.0$ , and  $\approx 2.7$  THz in agreement with non-resonant OKE (2.0 THz, Extended Data Figure 6), literature, and simulation (1.3 THz and 1.9 THz, Figure S7).



**Extended Data Figure 5 | Fitting TKE signals of Ag  $\beta$ -alumina.** Each signal (blue in **a**-**g**) was measured in a purged atmosphere and modeled as the sum of an instantaneous component (orange) and a single-exponential relaxation (green) (Supplementary Notes 1 and 2). For the thin sample (**e**-**h**), the instantaneous component was negligible. The Fourier transforms (**b****d****f****h**) of residuals (dark red), plotted with 0.1-THz Gaussian-filter smoothing, show a frequency component at  $\approx 1.2$  THz in agreement with literature (infrared-active mode at 1.0-1.2 THz) and simulation (1.0 THz, Figure S7). The signal is very similar between the thick and thin samples (Extended Data Figure 2), consistent with it arising from a thin layer of the material and consistent with strong absorption (Supplementary Note 3).



**Extended Data Figure 6 | Non-resonant optical Kerr effect in  $\beta$ -aluminas.** Schematic of the experimental configuration (a) and signals from thick Na (orange), K (purple), and Ag (dark red)  $\beta$ -alumina crystals (b) at positive time delays following a strong coherent artifact at zero time delay. The frequency components are extracted from linear prediction fitting results (Methods) shown as black dashed lines.

1. He, X., Zhu, Y. & Mo, Y. Origin of fast ion diffusion in super-ionic conductors. *Nat. Commun.* **8**, 1–7 (2017).
2. Gao, Y. *et al.* Classical and Emerging Characterization Techniques for Investigation of Ion Transport Mechanisms in Crystalline Fast Ionic Conductors. *Chem. Rev.* **120**, 5954–6008 (2020).
3. Ohno, S. *et al.* Materials design of ionic conductors for solid state batteries. *Prog. Energy* **2**, 022001 (2020).
4. Muy, S. *et al.* Tuning mobility and stability of lithium ion conductors based on lattice dynamics. *Energy Environ. Sci.* **11**, 850–859 (2018).
5. Krauskopf, T. *et al.* Comparing the Descriptors for Investigating the Influence of Lattice Dynamics on Ionic Transport Using the Superionic Conductor Na<sub>3</sub>PS<sub>4-x</sub>Se<sub>x</sub>. *J. Am. Chem. Soc.* **140**, 14464–14473 (2018).
6. Eyring, H. The Activated Complex and the Absolute Rate of Chemical Reactions. *Chem. Rev.* **17**, 65–77 (1935).
7. Evans, M. G. & Polanyi, M. Some applications of the transition state method to the calculation of reaction velocities, especially in solution. *Trans. Faraday Soc.* **31**, 875 (1935).
8. Maier, J. *Physical Chemistry of Ionic Materials: Ions and Electrons in Solids*. John Wiley & Sons, Ltd **1**, (John Wiley & Sons, Ltd, 2004).
9. Muy, S. *et al.* Lithium Conductivity and Meyer-Neldel Rule in Li<sub>3</sub>PO<sub>4</sub>-Li<sub>3</sub>VO<sub>4</sub>-Li<sub>4</sub>GeO<sub>4</sub> Lithium Superionic Conductors. *Chem. Mater.* **30**, 5573–5582 (2018).
10. Andersson, R., Årén, F., Franco, A. A. & Johansson, P. Ion Transport Mechanisms via Time-Dependent Local Structure and Dynamics in Highly Concentrated Electrolytes. *J. Electrochem. Soc.* **167**, 140537 (2020).
11. Funke, K., Cramer, C. & Wilmer, D. Concept of mismatch and relaxation for self-diffusion and conduction in ionic materials with disordered structures. in *Diffusion in Condensed Matter* 857–893 (Springer-Verlag, 2005). doi:10.1007/3-540-30970-5\_21
12. Poletayev, A. D., Dawson, J. A., Islam, M. S. & Lindenberg, A. M. Defect-Driven Anomalous Transport in Fast-Ion Conducting Solid Electrolytes. <https://arxiv.org/abs/2105.08761> (2021).
13. Song, S. *et al.* Transport dynamics of complex fluids. *Proc. Natl. Acad. Sci. U. S. A.* **116**, 12733–12742 (2019).
14. Klafter, J. & Sokolov, I. M. *First Steps in Random Walks*. (Oxford University Press, 2011). doi:10.1093/acprof:oso/9780199234868.001.0001
15. Seifert, U. Stochastic thermodynamics: From principles to the cost of precision. *Phys. A Stat. Mech. its Appl.* **504**, 176–191 (2018).
16. Sood, A. *et al.* Electrochemical ion insertion from the atomic to the device scale. *Nat. Rev. Mater.* **6**, 847–867 (2021).
17. Trinh, M. T. *et al.* Large polarons in lead halide perovskites. *Sci. Adv.* **3**, e1701217 (2017).
18. Bakulin, A. A. *et al.* Mode-selective vibrational modulation of charge transport in organic electronic devices. *Nat. Commun.* **6**, 7880 (2015).
19. Elgabarty, H. *et al.* Energy Transfer within the Hydrogen Bonding Network of Water Following Resonant Terahertz Excitation. *Sci. Adv.* **6**, 1–15 (2020).
20. Zalden, P. *et al.* Molecular polarizability anisotropy of liquid water revealed by terahertz-induced transient orientation. *Nat. Commun.* **9**, 1–7 (2018).
21. Von Hoegen, A., Mankowsky, R., Fechner, M., Först, M. & Cavalleri, A. Probing the

- interatomic potential of solids with strong-field nonlinear phononics. *Nature* **555**, 79–82 (2018).
22. Kozina, M. *et al.* Terahertz-driven phonon upconversion in SrTiO<sub>3</sub>. *Nat. Phys.* (2019). doi:10.1038/s41567-018-0408-1
  23. Neugebauer, M. J. *et al.* Comparison of coherent phonon generation by electronic and ionic Raman scattering in LaAlO<sub>3</sub>. *Phys. Rev. Res.* **3**, 13126 (2021).
  24. Först, M. *et al.* Nonlinear phononics as an ultrafast route to lattice control. *Nat. Phys.* **7**, 854–856 (2011).
  25. Hebling, J., Yeh, K.-L., Hoffmann, M. C. & Nelson, K. A. High-power THz generation, THz nonlinear optics, and THz nonlinear spectroscopy. *IEEE J. Sel. Top. Quantum Electron.* **14**, 345–353 (2008).
  26. Hoffmann, M. C. & Fülöp, J. A. Intense ultrashort terahertz pulses: Generation and applications. *J. Phys. D: Appl. Phys.* **44**, (2011).
  27. Colomban, P., Mercier, R. & Lucazeau, G. Vibrational study of and conduction mechanism in  $\beta$  alumina. II. Nonstoichiometric  $\beta$  alumina. *J. Chem. Phys.* **75**, 1388–1399 (1981).
  28. Colomban, P. & Lucazeau, G.  $\beta''$ -and ion-rich  $\beta$ -alumina: Comparison of vibrational spectra and conductivity parameters. *Solid State Ionics* **2**, 277–288 (1981).
  29. Hao, C. H., Chase, L. L. & Mahan, G. D. Raman scattering in beta-alumina. *Phys. Rev. B* **13**, 4306–4313 (1976).
  30. Chase, L. L., Hao, C. H. & Mahan, G. D. Raman scattering from sodium and silver in beta-alumina. *Solid State Commun.* **18**, 401–403 (1976).
  31. Klein, P. B., Schafer, D. E. & Strom, U. Cation interstitial pair modes in the vibrational spectra of mixed  $\beta$ -aluminas. *Phys. Rev. B* **18**, 4411–4421 (1978).
  32. Barker, A. S., Ditzenberger, J. A. & Remeika, J. P. Lattice vibrations and ion transport spectra in  $\beta$ -alumina. I. Infrared spectra. *Phys. Rev. B* **14**, 386–394 (1976).
  33. Allen, S. J., Cooper, A. S., Derosa, F., Remeika, J. P. & Ulas, S. K. Far-infrared absorption and ionic conductivity of Na, Ag, Rb, and K  $\beta$ -alumina. *Phys. Rev. B* **17**, 4031–4042 (1978).
  34. Savolainen, J., Ahmed, S. & Hamm, P. Two-dimensional Raman-terahertz spectroscopy of water. *Proc. Natl. Acad. Sci. U. S. A.* **110**, 20402–20407 (2013).
  35. Ciardi, G., Berger, A., Hamm, P. & Shalit, A. Signatures of Intra- and Intermolecular Vibrational Coupling in Halogenated Liquids Revealed by Two-Dimensional Raman-Terahertz Spectroscopy. *J. Phys. Chem. Lett.* **10**, 4463–4468 (2019).
  36. Hoffmann, M. C., Brandt, N. C., Hwang, H. Y., Yeh, K. Lo & Nelson, K. A. Terahertz Kerr effect. *Appl. Phys. Lett.* **95**, 1–4 (2009).
  37. Sajadi, M., Wolf, M. & Kampfrath, T. Transient birefringence of liquids induced by terahertz electric-field torque on permanent molecular dipoles. *Nat. Commun.* **8**, 1–8 (2017).
  38. Allodi, M. A., Finneran, I. A. & Blake, G. A. Nonlinear terahertz coherent excitation of vibrational modes of liquids. *J. Chem. Phys.* **143**, (2015).
  39. Zhu, H. *et al.* Screening in crystalline liquids protects energetic carriers in hybrid perovskites. *Science (80-. )*. **353**, 1409–1413 (2016).
  40. Fleischer, S., Zhou, Y., Field, R. W. & Nelson, K. A. Molecular orientation and alignment by intense single-cycle THz pulses. *Phys. Rev. Lett.* **107**, 1–5 (2011).
  41. Sajadi, M., Wolf, M. & Kampfrath, T. Terahertz-field-induced optical birefringence in common window and substrate materials. *Opt. Express* **23**, 28985 (2015).
  42. Maehrlein, S. F. *et al.* Decoding Ultrafast Polarization Responses in Lead Halide

- Perovskites by the Two-Dimensional Optical Kerr Effect. *Proc Natl Acad Sci USA* **19**, arxiv.org/abs/2008.06791 (2021).
43. Mishra, P. K., Vendrell, O. & Santra, R. Ultrafast Energy Transfer from Solvent to Solute Induced by Subpicosecond Highly Intense THz Pulses. *J. Phys. Chem. B* **119**, 8080–8086 (2015).
44. Mishra, P. K., Bettaque, V., Vendrell, O., Santra, R. & Welsch, R. Prospects of Using High-Intensity THz Pulses to Induce Ultrafast Temperature-Jumps in Liquid Water. *J. Phys. Chem. A* **122**, 5211–5222 (2018).
45. Whittingham, M. S. & Huggins, R. A. Electrochemical preparation and characterization of alkali metal tungsten bronzes,  $MxWO_3$ . in *Solid state chemistry—Proceedings of the 5th materials research symposium sponsored by the Institute for Materials Research, National Bureau of Standards* (eds. Roth, R. S. & Schneider S.J. Jr) 51–62 (1972).
46. Greenbaum, S. G. & Strom, U. Low-temperature nuclear spin relaxation in  $\beta$ -aluminas. *Solid State Commun.* **46**, 437–440 (1983).
47. Kamishima, O. *et al.* Temperature dependence of low-lying phonon dephasing by ultrafast spectroscopy (optical Kerr effect) in Ag  $\beta$ -alumina and Tl  $\beta$ -alumina. *J. Phys. Condens. Matter* **19**, 456215 (2007).
48. Hayes, W., Hopper, G. F. & Pratt, F. L. Ionic conductivity of potassium  $\beta''$  alumina in the very far infrared. *J. Phys. C Solid State Phys.* **15**, L675–L680 (1982).

# The Persistence of Memory in Ionic Conduction Probed by Nonlinear Optics: Supplementary Information

## Methods

Supplementary Note 1: Terahertz Kerr Effect (TKE)

Supplementary Note 2: TKE Control Measurements

Supplementary Note 3: Optical Conductivity from Terahertz Transmission

Supplementary Note 4: Pumped Molecular Dynamics

Supplementary Note 5: Attempt Frequencies in Na  $\beta$ -alumina

Figures S1-S10

Supplementary References 1-50

## Methods

### Sample Preparation

Single crystals of Na  $\beta$ -alumina were graciously shared with us by Prof. Osamu Kamishima. They were ion-exchanged to Ag and K in molten nitrates until no mass change was detectable, at least 3 days. For Ag, the process had to be repeated. For K, mixed nitrate compositions were used first to avoid mechanical damage from the thermodynamically favorable ion exchange. The  $c$  lattice constants for the Na, Ag, and K  $\beta$ -alumina samples were 22.53, 22.49, and 22.73 Å, respectively. Polycrystalline K  $\beta''$ -alumina was purchased from Ionotec Ltd as a pellet. To produce thin samples ( $\approx 5$ -30  $\mu\text{m}$ ), single crystals and the polycrystalline material were hand-polished using a T-tool, and then dried. Double-side polished sapphire (0001) was purchased from MTI Corp.

### Terahertz Kerr Effect (TKE)

The output of a Ti:sapphire oscillator (Coherent Micra) is amplified (Coherent Spitfire) to  $\approx 4.2$  mJ at 1 kHz, and pulse width optimized to maximize the peak terahertz field at the sample,  $\approx 150$  fs. 99% of the output is used to generate terahertz pulses ( $\approx 6$   $\mu\text{J}$ ) via optical rectification in lithium niobate using a tilted pulse front<sup>1,2</sup>. The terahertz pulse is focused on the sample using a pair of off-axis parabolic (OAP) mirrors. Peak field amplitudes at the sample position were  $\approx 700$  kV/cm in ambient atmosphere, and  $\approx 600$  kV/cm in purged ( $\leq 0.1\%$  RH) atmosphere. 1% of the amplifier output is used for the probe pulse, polarized at 45 degrees from the pump pulse, overlapped with the pump at the sample position, and passed through a quarter-wave plate and a Wollaston prism. The birefringence of the transmitted probe is measured with two photodiodes in a balanced detection scheme. The terahertz waveform at the sample position is measured with a free-standing uniaxially poled mixture of an electro-optic dye and amorphous polycarbonate polymer<sup>3,4</sup>, and the peak field strength measured by electro-optic sampling in GaP(110). The time delay between pump and probe pulses is varied with a mechanical delay stage. For measurements at elevated temperature, a transmission-mode heating stage (Linkam) was used without windows. The transient birefringence of ambient and purged air was measured by

aligning to a sample, and then removing the sample. The majority of experimental data is adapted from ADP's doctoral dissertation<sup>5</sup>.

### Terahertz Transmission

Thin ( $\leq 30 \mu\text{m}$ ) samples are mounted on thin metallic pinholes of diameter 1 mm, fully covering the pinhole. The terahertz pulse transmitted through the sample is focused with a second pair of OAP mirrors and sampled with the free-standing film of an electro-optic dye and amorphous polycarbonate polymer<sup>3,4</sup>. A time delay sweep of an empty pinhole is measured following every time delay sweep measuring the sample. Optical conductivity was fit to the time-domain spectra assuming a slab geometry<sup>6,7</sup> using a nonlinear fitting procedure with initial condition  $\tilde{n}=2+0.5j$ , which yielded stable fitting without the single-pass assumption.

### Optical Kerr Effect (OKE)

The output of a Ti:sapphire oscillator (Coherent Micra) was amplified (Coherent RegA) at 100 kHz to  $\approx 1 \mu\text{J}$  and compressed to  $\approx 50 \text{ fs}$  FWHM (the width of the coherent artifact in OKE). The pump and probe pulses were overlapped on the sample so that probe  $E \perp c$  crystal for single crystals, and pump  $\approx 15$  degrees off. The transmitted probe was detected using a pair of Si photodetectors in a balanced detection scheme. Frequencies of oscillatory components in the OKE signals were fit using linear prediction fitting<sup>8</sup>.

### Steady-State Molecular Dynamics (MD)

Steady-state classical MD simulations were carried out using LAMMPS<sup>9</sup> using Buckingham pairwise potentials as described previously<sup>10</sup>. The vibrational density of states was calculated from the velocity autocorrelation functions for the mobile ions, and the optical conductivity from the velocity autocorrelation function for the center of mass of the mobile ions<sup>11</sup>.

### MD with Pumping

An impulsive electrical field was included to mimic the experimental terahertz pulse<sup>12–15</sup>. Peak field  $E = 300 \text{ kV/cm}$  parallel to the conduction plane was used to account for  $\approx 50\%$  frequency-independent front-surface reflection. Charge-compensating defects were placed in the scaled-up simulations using the same procedure as described previously<sup>10</sup>. To sample hopping events, 800 randomized iterations per temperature point, with 4896 mobile ions each, were used for  $\beta$ -aluminas. For K  $\beta''$ -alumina, the simulations contained 5940 mobile ions each. Each iteration started with an anneal to 1000 K to further randomize starting positions of the mobile ions, and a short equilibration at the simulation temperature in the NVT ensemble. The electric field was applied in the NVE ensemble, and the simulations propagated for 15 ps, enough for mobile ions and the host lattice to come to the same temperature. For K  $\beta''$ -alumina, polycrystal orientations to match the experimentally available sample were averaged by changing the polarization of the simulated field over 12 angles in increments of 30 degrees. No significant dependence on the pump angle was observed in simulations of  $\beta$ -aluminas. The hopping statistics were extracted from all simulations and analyzed as described previously<sup>10</sup>. The direction of each hopping event was taken as the vector connecting the start and end crystallographic sites of the hop. The anisotropy of hopping was calculated by weighing the hopping directions by  $(\cos \theta)^2 - \langle (\cos \theta)^2 \rangle$ ,

with  $\theta$  the angle between the simulated pump field and the hop direction, and  $\langle(\cos \theta)^2\rangle = 0.5$  in the two-dimensional conduction plane.

## Supplementary Note 1: Terahertz Kerr Effect

The 2D terahertz Kerr effect measurement is a  $\chi^{(3)}$  measurement that relies on the third-order response function<sup>16,17</sup>:

$$R_{ijkl}^{(3)}(t_2, t_1) = \left(\frac{i}{\hbar}\right)^2 \text{tr}\langle\alpha_{ij}(t_2 + t_1)[\mu_k(t_1)[\mu_l(0), \rho]]\rangle$$

Here, the transition dipole moment operator  $\mu$  and polarizability operator  $\alpha$  act on the equilibrium density matrix  $\rho$  describing the thermal population of vibrational states. The pump pulses arrive at times 0 and  $t_1$ . The 800nm probe pulse at  $t_2+t_1$  is assumed to be short. Because we use one pump pulse, our experiment represents a line cut through the  $(t_1, t_2)$  space corresponding to  $t_1=0$ . The third-order polarization in the sample is given by the integral over pathways:

$$P_i(t) = \int \int dt_1 dt_2 R_{ijkl}(t_2, t_1) E_{probe,j}(t) E_{THz,k}(t - t_2) E_{THz,l}(t - t_2 - t_1)$$

This formalism includes all possible two-photon excitation pathways via either bound vibrational states, virtual states (Raman), or “thermal bath” states<sup>16,17</sup>. The generated field is the time derivative of the generated polarization<sup>18–20</sup>:

$$E_i(t) \propto \frac{dP_i(t)}{dt}$$

Models of coherently excited vibrational responses utilize an oscillatory form of the generated polarization corresponding to a bound vibrational state, including possible anharmonic potential energy surfaces<sup>20,21</sup>, anharmonic couplings to other vibrations<sup>16,22</sup>, or couplings to a thermal bath<sup>15,23</sup>. For such an oscillating polarization, the detected change in the probe field at any time is proportional to the velocity of the oscillator. This formalism does not impose a coherence requirement or a functional form on the trajectory of the oscillator. In principle, this treatment should be valid for e.g. a Debye relaxation<sup>15</sup> or an ensemble of double-well oscillators coupled to a thermal bath. The first yields a “tail” response in the transient birefringence of liquids, while the second can model ionic hopping in the solid state. In such a model, the detected third-order signal is proportional to the transient anisotropy of the hopping rate, measured as a function of the pump-probe time delay. The pump-probe time delay is  $t_2$  in the above formalism and for simplicity is denoted as  $\Delta t$  in the main text and Figure 1.

For mismatched group velocities between the pump and probe pulses, the probe signal is the sum of generated fields along the position  $x = \Delta v_g \Delta t$  along the path of the pulses, where  $\Delta v_g$  is the mismatch of the group velocities of the pump and probe pulses<sup>20,24–26</sup>. For a terahertz pump and 800 nm probe in a sample mostly composed of alumina, refractive indices are taken as  $n_{probe} \approx 1.76$ , and  $n_{pump} \approx 3.08$ <sup>24,27</sup>, i.e. the probe propagates faster than the pump inside the sample. For  $\Delta t < L/\Delta v_g$ , where  $L$  is the thickness of the sample, the probe overtakes the pump within the sample, and samples the instantaneous electronic polarization. Ignoring the absorption of the pump pulse, and for the probe pulse assumed short, the strength of this signal is proportional to

the thickness of the sample convoluted with the square of the pump field and the nonlinear refractive index of the sample<sup>24</sup>. In fitting the TKE signals of  $\beta$ -aluminas and K  $\beta$ "-alumina, this component is referred to as the "instantaneous component".

## Supplementary Note 2: TKE Control Measurements

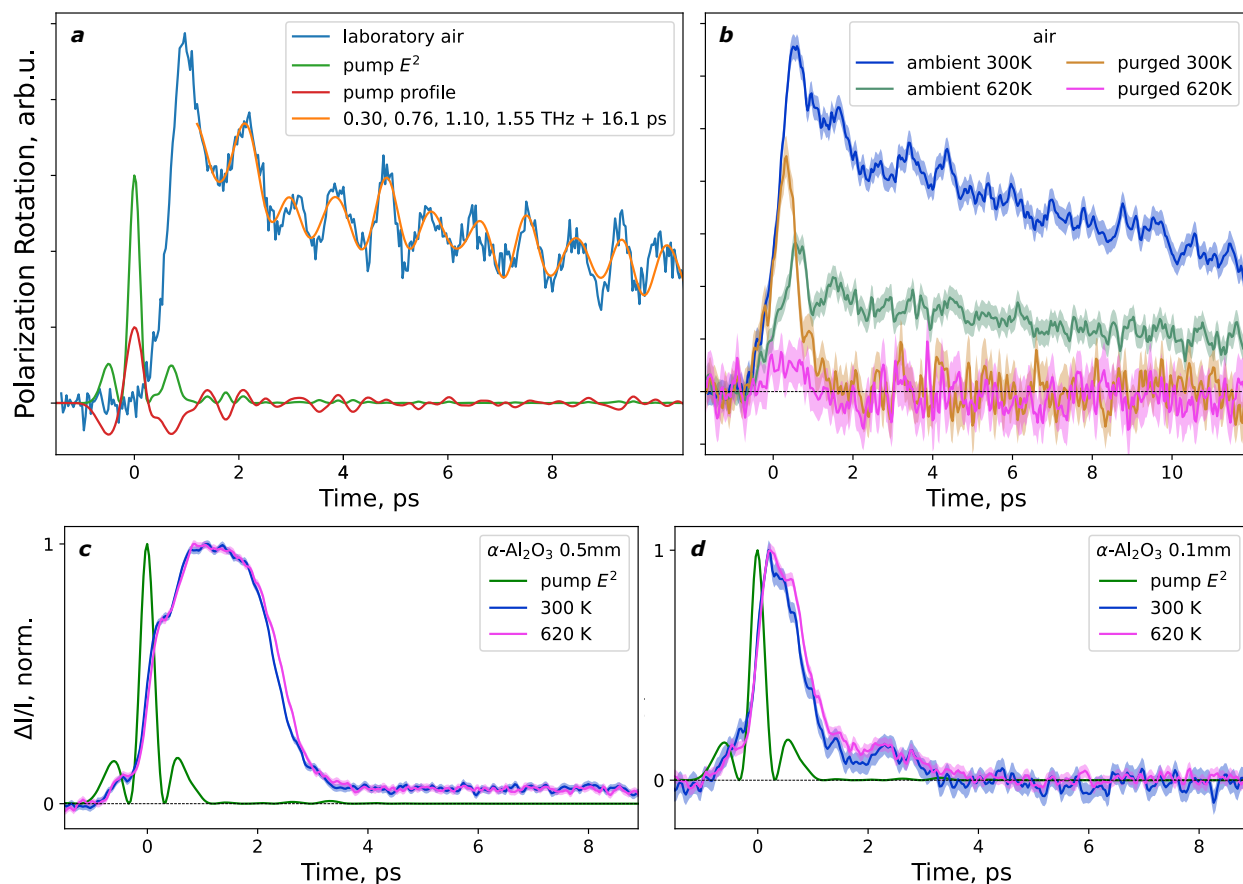


**Figure S1 | Terahertz Kerr effect (TKE) in control samples.** (a) TKE signal of ambient air (blue), and linear prediction fitting of oscillatory components (orange). (b) TKE signals of ambient air at 300 K (blue), purged air at 300 K (ochre), and ambient and purged air at 620 K (green and pink, respectively). The cited temperature is the temperature of the heating stage, with the pump and probe pulses passing through an opening in it. (c) TKE of 0.5 mm thick sapphire at 300 K (blue) and 620 K (pink). (d) TKE of 0.1 mm thick sapphire at 300 K (blue) and 620 K (pink). In (b-d), the shaded regions represent  $\pm 1$  s.e. of the mean.

Figure S1 shows TKE measurements of ambient air and sapphire samples. The TKE of ambient air shows a signal with components matching the absorption lines of water vapor at  $\approx 0.76$  THz and  $\approx 1.1$  THz<sup>28</sup>. This signal decreases by  $\approx$ half when the absolute temperature is  $\approx$ doubled (Figure S1b), and disappears entirely when the volume of pump-probe spatial overlap is purged with dry nitrogen, independent of temperature (Figure S1b). We therefore assign this signal to the rotational coherences of gas-phase atmospheric moisture. The strength of the rotational coherence of atmospheric nitrogen at  $\approx 8.4$  ps (Figures 1c and 2a, main text) also decreases by

approximately half, relative to the remainder of the signal, upon heating from 300 K to 620 K.

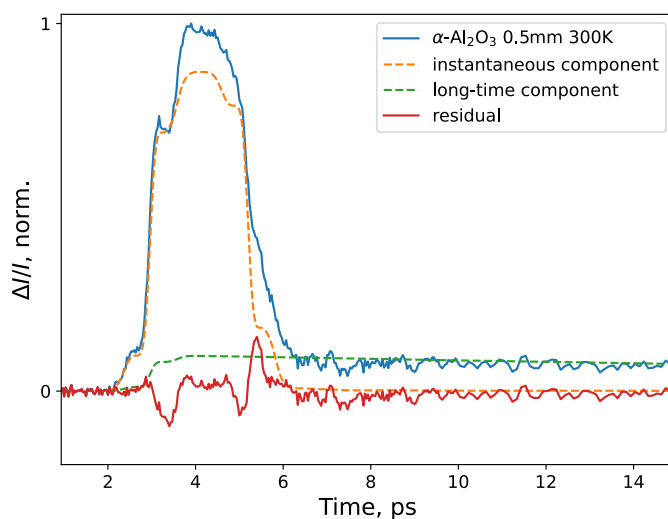


**Figure S2 | TKE signal from 0.5-mm sapphire (0001) at 300 K.** The TKE signal (blue) is fit to the sum of an instantaneous component (orange) and a long-time component that appears simultaneously. The residual is plotted in red. The rotational coherence of atmospheric nitrogen is at  $\approx 11.4$  ps with the peak pump field at  $\approx 3$  ps.

The TKE signals from sapphire samples (Figure S1cd) measured in purged atmosphere are temperature-independent. The sapphire signal is modeled (Figure S2) as a combination of an instantaneous component (Supplementary Note 1 and Ref. <sup>24</sup>) and a long-time component that is absent in the 0.1-mm sample (Figure S1d). Since the long-time components (“tails”) in the TKE signals of  $\beta$ -aluminas are, unlike for sapphire, thickness-independent, but ion- and temperature-dependent, their origin must be distinct from that of the long-time sapphire signal. A more exact model of the sapphire signals remains possible, but the simpler one suffices here.

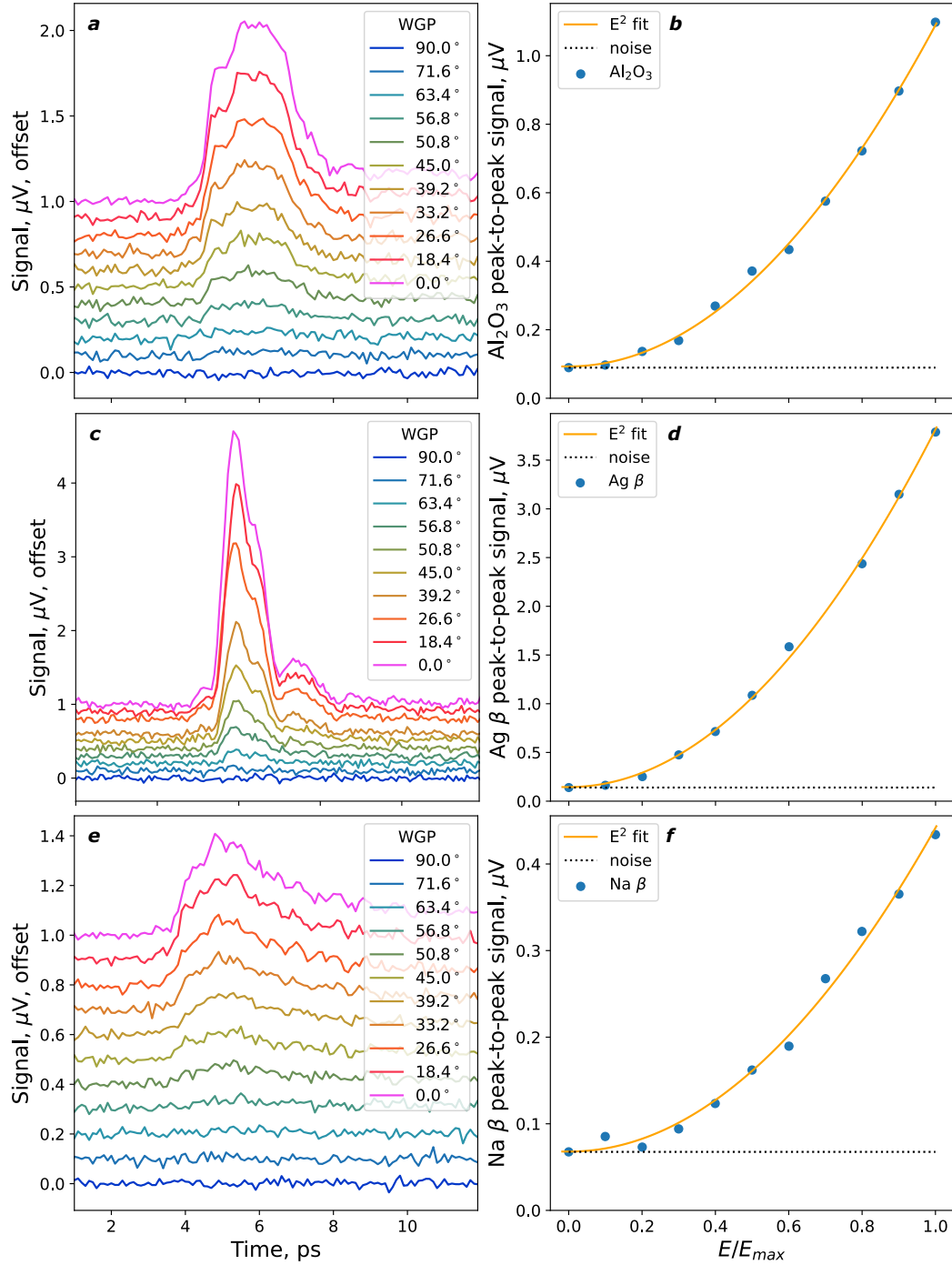


**Figure S3 | Pump field dependence of TKE signals.** Time-domain TKE signals as functions of wire-grid polarizers (WGP) angle for 0.5-mm sapphire (a),  $\approx 0.4$ -mm Ag  $\beta$ -alumina (c), and  $\approx 0.4$ -mm Na  $\beta$ -alumina (e). The pump field is maximum at the zero degrees position of the WGP, and the pump is fully blocked at 90 degrees. The peak-to-peak signals for sapphire (b), Ag  $\beta$ -alumina (d), and Na  $\beta$ -alumina (f) with fits (orange) to a noise level (dotted) and the intensity of the THz pump field.

All TKE signals scale with the peak intensity of the THz pump field (Figure S3). Whenever they are measurable, the kinetics of the relaxation are independent of the pump field strength.

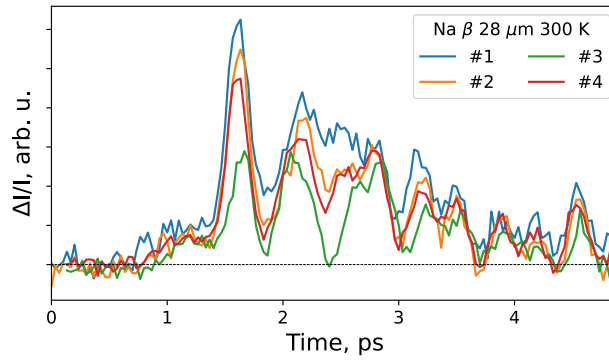


**Figure S4 | Stability of the TKE signal in Na  $\beta$ -alumina.** TKE in a thin sample of Na  $\beta$ -alumina, measured four times (#1 through #4 chronologically) over  $\approx 4$  days with other measurements in between. There was a pause between the third and fourth measurements. Here, the peak pump field is applied at 1.5 ps.

The TKE signals in  $\beta$ -aluminas show deviations at short time delays upon prolonged (several days) measurements (Figure S4), which can be reversed by stopping measurements. The measurements presented in the main text are taken when such effects are minimized, e.g., on fresh samples. The changes over the course of each measurement, up to  $\approx 12$  hours, are small, and the long-time-delay components of the signals are unaffected.

### Supplementary Note 3: Optical Conductivity from Terahertz Transmission

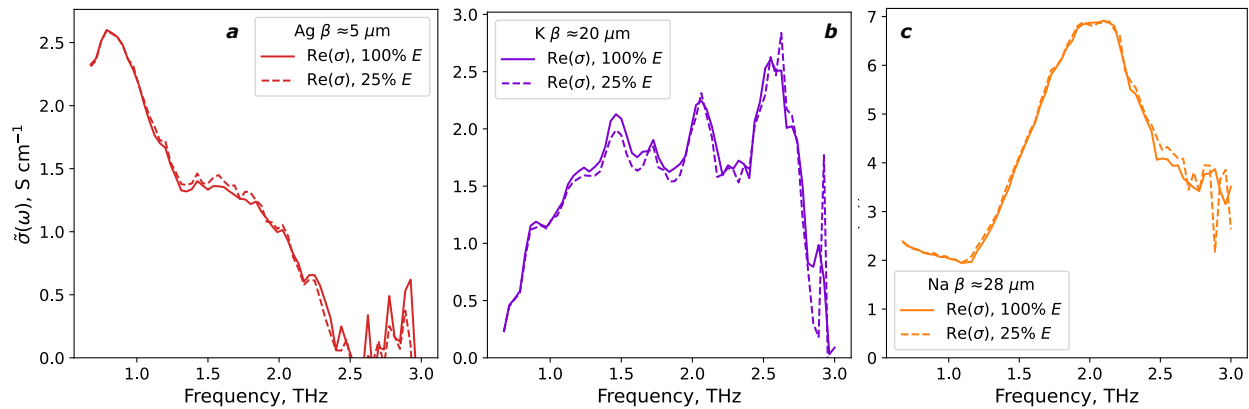


**Figure S5 | Optical conductivity of  $\beta$ -aluminas in the far infrared.** Real part of the optical conductivity  $\sigma$ , calculated from terahertz transmission through single-crystalline Ag (**a**, dark red), K (**b**, purple), and Na (**c**, orange)  $\beta$ -aluminas. The thicknesses of samples used are noted in the legends. The relative uncertainties in the absolute values due to the choice of starting fit guess are  $\leq 50\%$ . For each, the transmission measurements were performed at  $\geq 500$  kV/cm (denoted as 100%  $E$  field, solid lines) and a quarter of that (denoted as 25%  $E$  field, dashed lines). In all cases, the polarization of the pump field was parallel to the conduction planes of the crystals. Below  $\approx 0.7$  THz, and above  $\approx 2.8$  THz, the transmission was weak and conductivity calculations noisy.

The complex refractive index  $\tilde{n}(\omega)$  was fit to the transmission at each frequency<sup>6,7,29</sup>. For a free-standing slab of thickness  $L$ , the transmission  $T(\omega)$  relative to a pinhole reference is given as:

$$T(\omega) = \frac{4\tilde{n}(\omega)}{(\tilde{n}(\omega) + 1)^2} \exp(ikL(\tilde{n}(\omega) - 1))$$

Here,  $k$  is the wavenumber equal to  $\omega/c$ . This nonlinear equation was solved for  $\tilde{n}(\omega)$  at each frequency provided an initial guess  $\tilde{n}_0(\omega)$ ; the values shown in Figure S5 use  $\tilde{n}_0 = 2+0.5i$ . The relative uncertainty due to choices of  $\tilde{n}_0$  is  $\leq 50\%$ , but the solver is robust to small uncertainties in other inputs, such as possible variation or e.g. 20% error in the sample thickness. This method also avoids the simplifying single-pass assumption.

The optical conductivities of  $\beta$ -aluminas show features and absolute magnitudes consistent with literature spectra of melt-grown crystals<sup>30</sup>:  $\approx 0.8$  THz in Ag  $\beta$ -alumina, 2.1 THz in Na  $\beta$ -alumina, and several modes between 1.5, 2.0, and 2.7 THz in K  $\beta$ -alumina. More importantly, for all conditions and all samples the calculated refractive index and conductivity are independent of the terahertz field for the same  $\tilde{n}_0$  used to solve. No field-strength-dependent shifting or bleaching of any features are observed over multiple measurements of each sample.

#### Supplementary Note 4: Pumped Molecular Dynamics

The selective excitation of mobile-ion motions in  $\beta$ -aluminas is verified with simulations including the pump field. During the simulated terahertz pump pulse, the temperature of the mobile ions, computed by LAMMPS using the kinetic energy of the ions, rises rapidly (Figure S6ac). After the pulse is turned off, the temperature of the mobile ions begins to decrease, and the temperature of the host lattice species increases. For all materials, the terahertz pulses selectively deposit energy into the mobile ions, which then thermalize with the lattice on a picosecond timescale. The timescale of this thermalization is substantially longer than that of the relaxation of anisotropy in hopping, highlighting the selectivity of the nonlinear optical measurement to the directional alignment of hopping.

The excitation of vibrational modes by the pump pulse, in addition to hopping, is verified by tracking the displacements of the center of mass of the mobile ions, projected onto the direction of the field, and referenced to the host-lattice displacement<sup>31</sup>. Simplifying the ensembles of mobile ions and the host lattice to two point charges, the emitted field from coherent oscillations excited by the pump should be proportional to the velocity of the relative center-of-mass motions. This yields several material-specific vibrations (Figure S7) with frequencies typically within 10-20% of known literature infrared- and Raman-active vibrations<sup>30,32–38</sup>. For example, simulated vibrations are 0.6 and 1.0 THz in Ag  $\beta$ -alumina, and 1.7 THz in Na  $\beta$ -alumina. For simulated K  $\beta$ -alumina, the vibration at  $\approx 1.3$  THz is only excited at 300 K, while the vibration at  $\approx 2.0$  THz is excited at both 300 K and 600 K, in agreement with the TKE experiment (main text Figure 2b). For a classical simulation that does not account for partial covalency, this is excellent agreement. The simulated coherent displacements of the mobile-ion center of mass are between 5-15 picometers during the application of the pulse, in line with terahertz-frequency pump-probe studies in solid-state materials<sup>20,21,39</sup>.

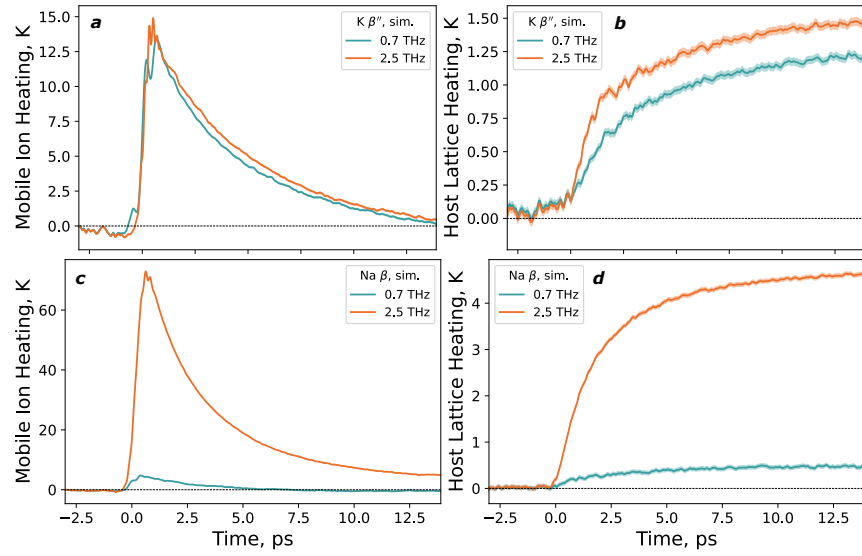


**Figure S6 | Heating of  $\beta''$ - and  $\beta$ -aluminas by simulated terahertz pulses.** (a,b) Simulated temperature rise in  $K\beta''$ -alumina: mobile ions (a) and the host lattice (b) with electric field pulses at 0.7 THz (teal) and 2.5 THz (orange). (c,d) Simulated temperature rise in  $Na\beta$ -alumina: mobile ions (c) and the host lattice (d) with electric field pulses at 0.7 THz (teal) and 2.5 THz (orange). The shaded areas are  $\pm 1$  s.e. of the mean.

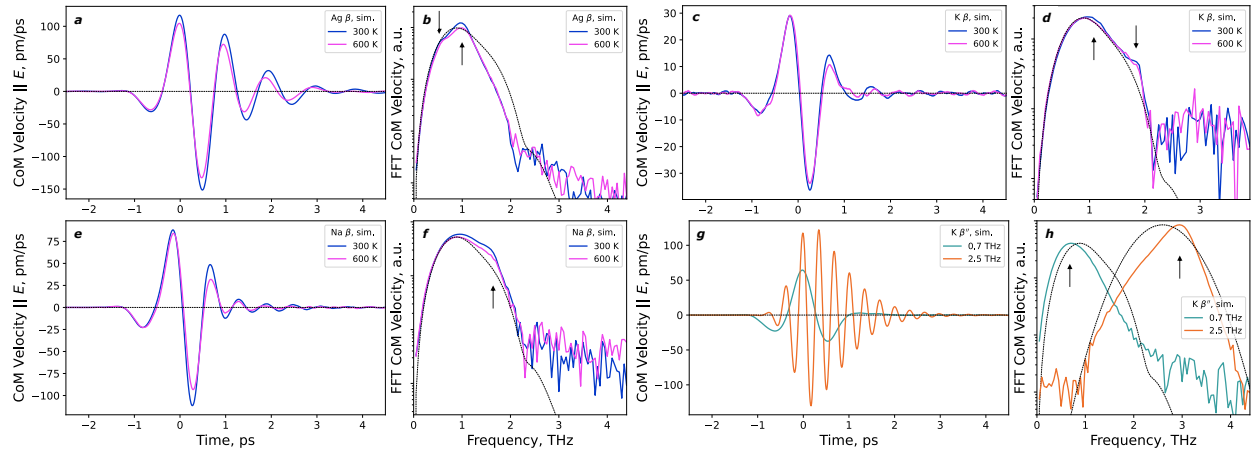


**Figure S7 | Simulated excitation of coherent motions of mobile ions by terahertz pumps.** Velocities of the center-of-mass of all mobile ions (a,c,e,g), and their Fourier transforms (b,d,f,h). Dashed black lines in the Fourier transform figures are spectra of the applied pump pulses. Highlighted vibrations: 0.6 and 1.0 THz in  $Ag\beta$ -alumina (a,b), 1.3 and 2.0 THz in  $K\beta$ -alumina (c,d), 1.7 THz in  $Na\beta$ -alumina (e,f), and 3.0 THz in  $K\beta''$ -alumina (g,h).

The *in silico* TKE of  $\beta$ -aluminas is dis-aggregated by the chemical environment of the mobile ions: bound in a defect cluster, and free to diffuse. The cluster consists of four mobile ions on six crystallographic lattice sites around an oxygen interstitial<sup>10,40,41</sup>. These ions shift between the sites within the cluster. The hopping components of *in silico* TKE of  $Na\beta$ -alumina (Figure S8) are

similar at short time delays (Figure S8bc) – but only the un-bound ions yield anisotropic hopping past 1 ps (Figure S8b). This response is also weakly thermally activated.

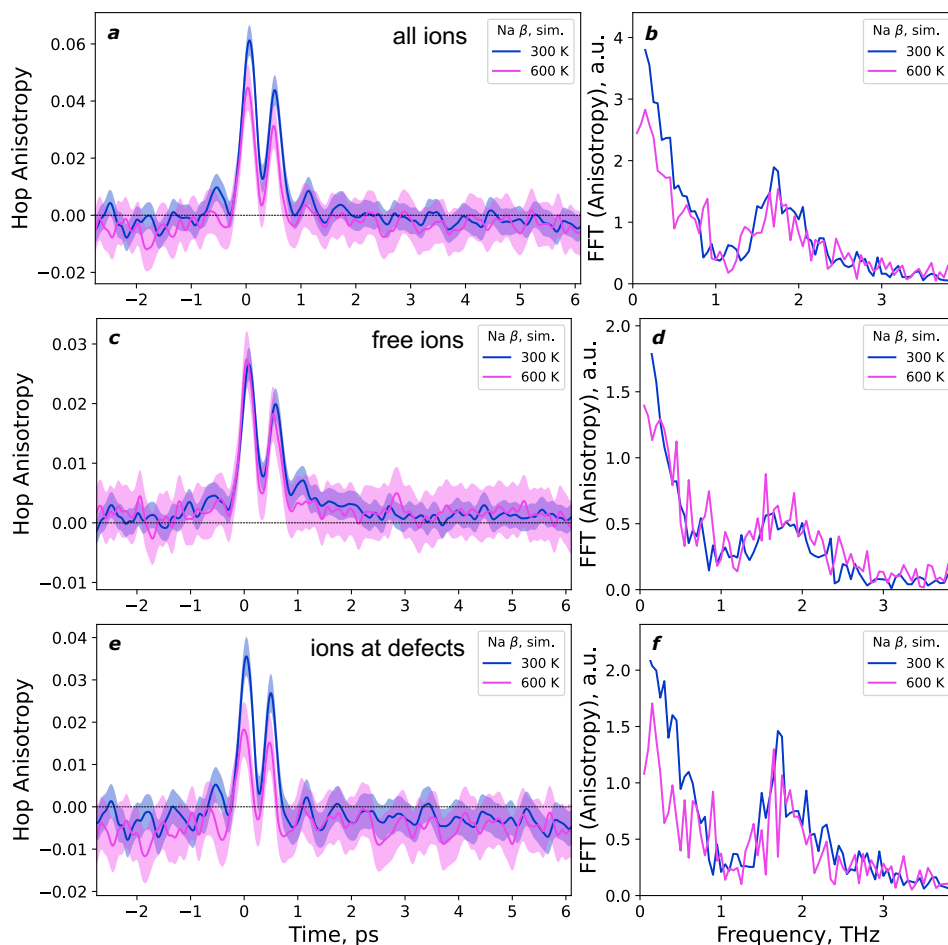


**Figure S8 | Temperature dependence of the simulated hopping anisotropy in Na  $\beta$ -alumina.** (ab) all mobile ions, (cd) mobile ions away from defects, i.e. “free”, and (ef) mobile ions within defect clusters. The shaded areas are  $\pm 1$  s.e. of the mean.

The temperature-independence of the hopping anisotropy response due to cluster-bound ions complicates the interpretation of experimental TKE measurements of Na and Ag  $\beta$ -aluminas (Figure 1cd). Additionally, the relaxation time constants are faster than in K  $\beta$ -alumina (Extended Data Figures 3-5). By analogy with high-frequency NMR relaxation<sup>42,43</sup>, the temperature activation of the back-hopping in Na and Ag  $\beta$ -aluminas is expected to be weaker than in K  $\beta$ -alumina. We focus on the K  $\beta$ -alumina signals because they possess stronger activation, more distinguishable time constants, and simpler interpretation due to the lack of a simulated response from the defect clusters in that material. At the same time, the agreement between the classical molecular dynamics simulation of K  $\beta$ -alumina and the low-frequency conductivity is the worst of all  $\beta$ -aluminas<sup>10</sup>. We believe this is due to the inability of the simulation to accurately describe the two-coordinate K environment at the anti-Beevers-Ross sites, which leads to an overestimation of activation energy and overall lower conductivity. This is consistent with the pumped molecular dynamics simulations also under-estimating the lifetimes of ions in high-

energy sites, and predicting a faster than experimental relaxation. However, the qualitative experiment-simulation agreement spans the existence, temperature-, frequency- and material-dependences. A more quantitative correspondence between simulation and experiment will require *ab initio* methods.

### Supplementary Note 5: Attempt Frequencies in Na $\beta$ -alumina

Here, we seek to understand the fundamental initiation of ion transport, the attempt frequency for ionic hopping. However, due to the presence of defect clusters and non-equivalent crystallographic sites, the response of  $\beta$ -aluminas to electrical fields driving hops is more complex than for K  $\beta''$ -alumina (Figure 3ef). We first analyze steady-state simulations, followed by *in silico* TKE second. We focus on the hops into the high-energy anti-Beevers-Ross (aBR) sites from the low-energy Beevers-Ross (BR) sites. As chemical doping furthermore creates distinct chemical environments for the mobile ions, here we simulate the compositional  $\text{Na}_{1+2x}\text{Al}_{11}\text{O}_{17+x}$  series for  $\text{Na}_2\text{O}$  doping  $x=0,0.01,0.1$ , where the practical material corresponds to  $x=0.1$ .

For a molecular dynamics simulation, we partition the trajectories of mobile ions (typically, 100 ns for steady-state simulations) into hopping events, defined as the time point when an ion migrates between crystallographic lattice sites, and the residence times between them. A residence time is defined as the period of time that an ion spends at a lattice site following a hop into that site<sup>10</sup>. Here, we quantify the distributions of hopping residence times in the short-time, picosecond regime. If an ion is found to preferentially commit a hop for some (short) residence times corresponding to a multiple of some well-defined period, then such a period is empirically the inverse of the attempt frequency for hopping. Similarly, for any crystallographic site within the material, the times that elapse between an ion leaving it, and a new ion entering the site, “filling times” for short, can be analyzed with this statistical method.

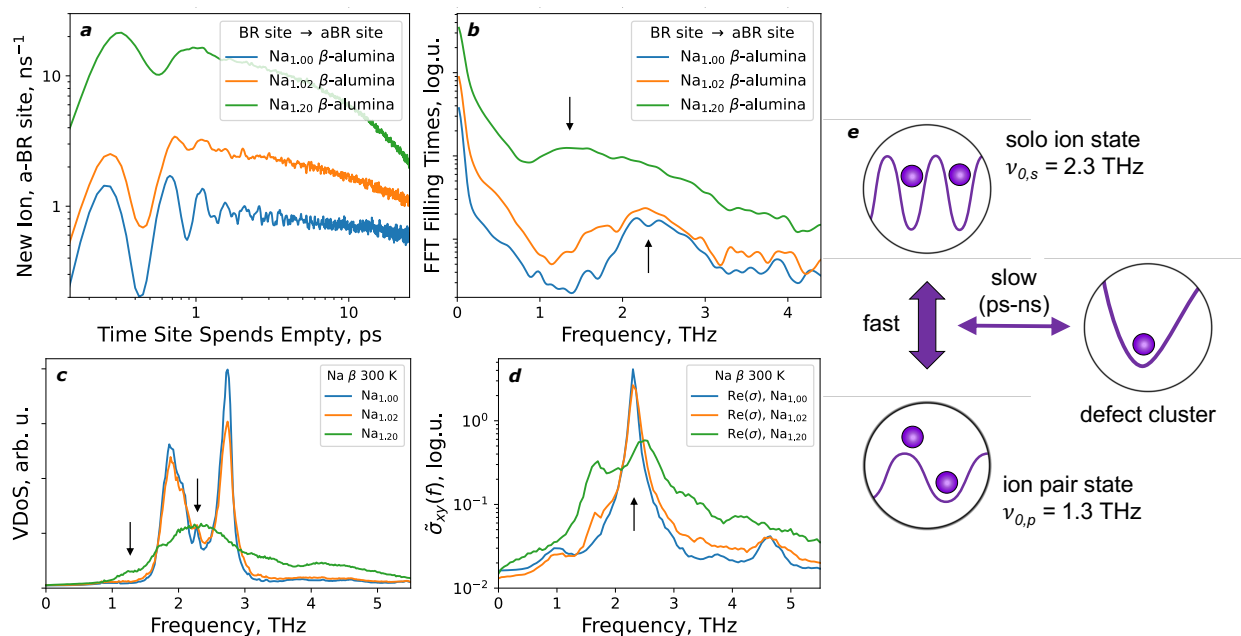


**Figure S9 | Attempt frequency analysis for Na  $\beta$ -alumina from MD simulations.** (a) Distributions of times that anti-Beevers-Ross sites spend empty following a Na ion hopping away, simulated at 600 K for  $x=0,0.01,0.1$  in stoichiometries  $\text{Na}_{1+2x}\text{Al}_{11}\text{O}_{17+x}$  (blue, orange, and green, respectively). (b) Fourier transforms of the distributions in (a), smoothed with a Gaussian filter of 0.1 THz st. dev. Arrows highlight peaks at 2.3 THz and 1.3 THz corresponding to the short-time structure of the distributions in (a). (c) Na vibrational density of states and (d) real part of the optical conductivity for the three simulated stoichiometries of Na  $\beta$ -alumina, with arrows highlighting the same frequencies as in (b). (e) Model of the three internal states for mobile ions in Na  $\beta$ -alumina: solo as in the defect-free ( $x=0$ ) material, part of an mobile-ion pair, and part of a defect cluster. The first two states possess distinct attempt frequencies for hopping, 2.3 THz and 1.3 THz, respectively, whereas the defect cluster is non-diffusing.

For the defect-free material,  $x=0$ , distributions of “filling times” for high-energy aBR sites (Figure S9a, blue) show preferential hops into the sites at periods of time corresponding to 2.3 THz (Figure S9b, blue), which is a minuscule yet distinct part of the Na vibrational density of states (Figure S9c, blue) and the main feature of the infrared conductivity (Figure S9d, blue). We conclude that 2.3 THz is the attempt frequency for  $\text{BR} \rightarrow \text{aBR}$  hopping in absence of neighboring Na ions already in aBR sites. This matches the experimentally measured infrared-active vibration at 2.0-2.1 THz. Adding even a single defect cluster per 100 formula units ( $x=0.01$ ) increases the rates of hopping and already changes the frequency makeup of the hopping attempts towards lower frequencies (Figure S9b, orange). The additional Na ion locates on the high-energy sites, and necessarily perturbs the energetics of its neighbors, resulting in interstitialcy diffusion<sup>44</sup> that originates with perturbed, softer attempt frequencies. The apparent softening of the attempt frequency with stoichiometric addition of Na ions to high-energy sites must result from the repulsions between mobile ions. For the practical simulated stoichiometry,  $x=0.1$ , the distribution of site filling times shows a longer period at short times (Figure S9a, green), which corresponds to the practical attempt frequency of 1.3 THz. This vibration is the attempt frequency for interstitialcy knock-on hopping in the practical Na  $\beta$ -alumina, with the simulated frequency corresponding to one measurable with inelastic neutron scattering at 1.2 THz<sup>45</sup>. The simulated vibrations at 1.3 and 2.3 THz (1.2 and 2.1 THz experimentally), are attempt frequencies for hopping from two distinct states (Figure S9e) via two mechanisms: interstitialcy ion-pair and solo, respectively. While both are present in the real material, the majority of transport occurs via the interstitialcy state.

Both vibrations are distinct from the LO phonon mode at 3.0 THz detectable by TKE (Figure 1), OKE (Extended Data Figure 6) and neutron scattering<sup>45</sup>, which was previously thought to correlate to hopping and activation energy<sup>46–48</sup>. The 1.3 THz attempt frequency corresponds to the interstitialcy nearest-neighbor mobile-ion pair created by chemical doping, whereas the 2.3 THz frequency is the attempt frequency for  $\text{BR} \rightarrow \text{aBR}$  hopping in absence of nearby Na ions already in aBR sites (Figure S9e). This softening of the attempt frequency with doping demonstrates the role of repulsions between mobile ions in driving ionic conductivity. Indeed, chemical doping alters not only the concentrations of the active species, but also the very energetics of each hop. Finally, the practical attempt frequency of 1.3 THz comprises only a minor part of both the Na vibrational density of states (Figure S9c) and simulated Na optical conductivity

(Figure S9d). By contrast, the optical phonon at 3.0 THz does not contribute to hopping, the same way that higher-frequency modes in  $K\beta''$ -alumina also do not contribute (main text, Figure 3ef). Overall, our statistical analysis enables a detailed examination of the vibrational contributions to hopping beyond average descriptors such as the mobile-ion phonon band center<sup>49,50</sup>.

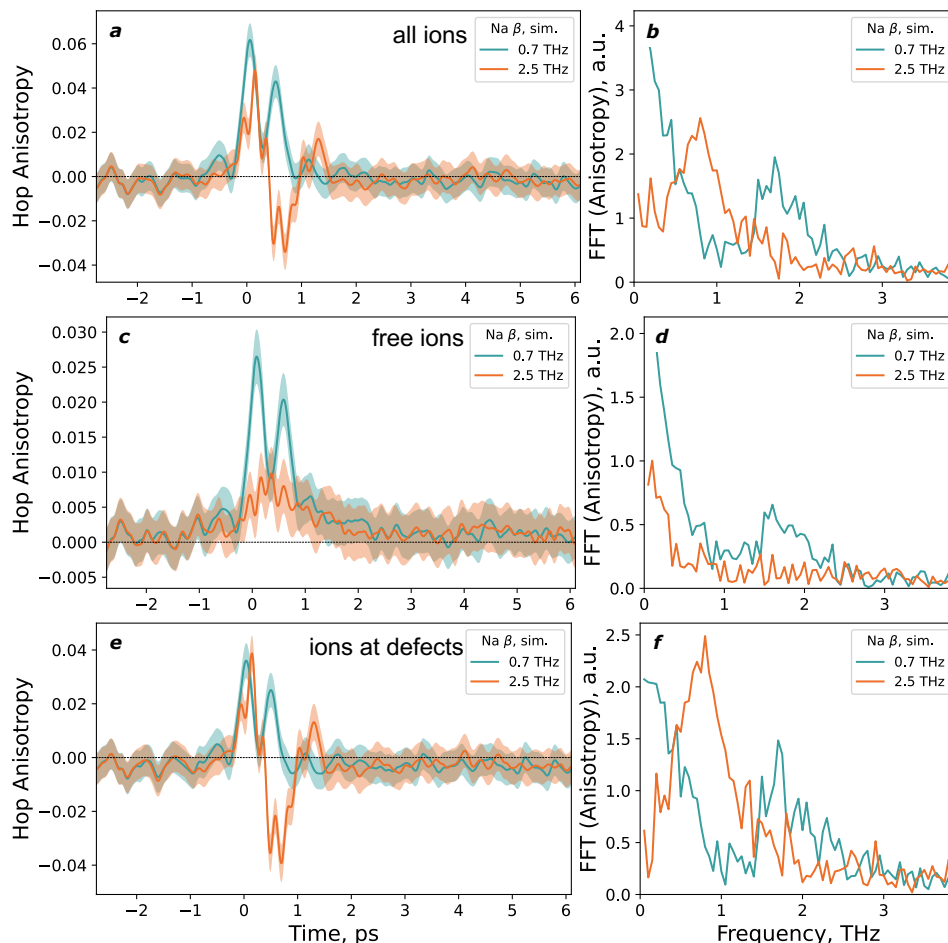


**Figure S10 | Simulated anisotropy of hopping in Na  $\beta$ -alumina at 300 K.** Time traces with the peak applied fields at zero time (**ace**), and Fourier transforms of the hopping anisotropy (**bdf**). Two pump pulses are compared: 0.7 THz (teal) repeated from Figure S8, and 2.5 THz (orange). The full response (**ab**) is dis-aggregated to the response of unbound ions (**cd**) and ions bound within defect clusters (**ef**). The shaded areas are  $\pm 1$  s.e. of the mean.

We now simulate an *in silico* TKE experiment for Na  $\beta$ -alumina, at the practical stoichiometry  $x=0.1$  and 300 K. Given two distinct mechanisms of hopping (Figure S9e) with two attempt frequencies, each of which could yield hopping when pumped. As for  $K\beta''$ -alumina (main text Figure 3ef), pump field frequencies of 0.7 THz and 2.5 THz are simulated at peak fields 300 kV/cm. The simulated 2.5 THz pulse raises the temperature of the system by  $\approx 4.5$  K, 10x more than the 0.7 THz pulse at  $\approx 0.45$  K (Figure S6cd). The hopping anisotropy in response to the simulated pumps (Figure S10) depends strongly both on the pumping frequency and on the location of the mobile ion (cluster-bound vs free). The response of free ions to the 2.5-THz pulse is distinct from

zero, but relatively weak given the strong absorption. The simulated 2.5-THz pulse excites the 2.3 THz attempt frequency and yields a signal in free ions (Figure S10b), although the signal is weak if accounting for the strong absorption. This is consistent with the hopping mechanism with the 2.3-THz attempt frequency providing only a minor contribution in the practical material. Finally, the overall hopping anisotropy response is strongly convoluted by defect clusters (Figure S10c). Overall, our simulation shows that TKE results should be interpreted with care for materials with multiple possible hopping mechanisms and internal states. Knowledge of the local environments of mobile ions is required to rigorously characterize the possible attempt frequencies in ionic conductors. We focus on the  $K\beta''$ -alumina in the main text for simplicity.

### Supplementary References

1. Hebling, J., Yeh, K.-L., Hoffmann, M. C. & Nelson, K. A. High-power THz generation, THz nonlinear optics, and THz nonlinear spectroscopy. *IEEE J. Sel. Top. Quantum Electron.* **14**, 345–353 (2008).
2. Hoffmann, M. C. Nonlinear Terahertz Spectroscopy. in *Terahertz Spectroscopy and Imaging* **171**, 355 (Springer-Verlag, 2013).
3. Zheng, X., Sinyukov, A. & Hayden, L. M. Broadband and gap-free response of a terahertz system based on a poled polymer emitter-sensor pair. *Appl. Phys. Lett.* **87**, 87–89 (2005).
4. McLaughlin, C. V., Zheng, X. & Hayden, L. M. Comparison of parallel-plate and in-plane poled polymer films for terahertz sensing. *Appl. Opt.* **46**, 6283–6290 (2007).
5. Poletayev, A. D. Ion Conduction By The Picosecond: Optical Probes and Correlations. (Stanford University, 2020).
6. Neu, J. & Schmuttenmaer, C. A. Tutorial: An introduction to terahertz time domain spectroscopy (THz-TDS). *J. Appl. Phys.* **124**, (2018).
7. Morimoto, T. *et al.* Microscopic ion migration in solid electrolytes revealed by terahertz time-domain spectroscopy. *Nat. Commun.* **10**, (2019).
8. Barkhuijsen, H., de Beer, R., Bovée, W. M. M. J. & van Ormondt, D. Retrieval of frequencies, amplitudes, damping factors, and phases from time-domain signals using a linear least-squares procedure. *J. Magn. Reson.* **61**, 465–481 (1985).
9. Plimpton, S. Fast Parallel Algorithms for Short-Range Molecular Dynamics. *J. Comput. Phys.* **117**, (1995).
10. Poletayev, A. D., Dawson, J. A., Islam, M. S. & Lindenberg, A. M. Defect-Driven Anomalous Transport in Fast-Ion Conducting Solid Electrolytes. <https://arxiv.org/abs/2105.08761> (2021).
11. Edvardsson, S., Ojamae, L. & Thomas, J. O. A study of vibrational modes in Na<sup>+</sup> beta-alumina by molecular dynamics simulation. *J. Phys. Condens. Matter* **6**, 1319–1332 (1994).
12. Mishra, P. K., Vendrell, O. & Santra, R. Ultrafast Energy Transfer from Solvent to Solute Induced by Subpicosecond Highly Intense THz Pulses. *J. Phys. Chem. B* **119**, 8080–8086 (2015).
13. Mishra, P. K., Bettaque, V., Vendrell, O., Santra, R. & Welsch, R. Prospects of Using High-Intensity THz Pulses to Induce Ultrafast Temperature-Jumps in Liquid Water. *J. Phys. Chem. A* **122**, 5211–5222 (2018).
14. Zalden, P. *et al.* Molecular polarizability anisotropy of liquid water revealed by terahertz-induced transient orientation. *Nat. Commun.* **9**, 1–7 (2018).
15. Elgabarty, H. *et al.* Energy transfer within the hydrogen bonding network of water following resonant terahertz excitation. *Sci. Adv.* **6**, eaay7074 (2020).

16. Finneran, I. A., Welsch, R., Allodi, M. A., Miller, T. F. & Blake, G. A. 2D THz-THz-Raman Photon-Echo Spectroscopy of Molecular Vibrations in Liquid Bromoform. *J. Phys. Chem. Lett.* **8**, 4640–4644 (2017).
17. Finneran, I. A. *et al.* Coherent two-dimensional terahertz-terahertz-Raman spectroscopy. *Proc. Natl. Acad. Sci. U. S. A.* **113**, 6857–6861 (2016).
18. Savolainen, J., Ahmed, S. & Hamm, P. Two-dimensional Raman-terahertz spectroscopy of water. *Proc. Natl. Acad. Sci. U. S. A.* **110**, 20402–20407 (2013).
19. Ciardi, G., Berger, A., Hamm, P. & Shalit, A. Signatures of Intra- and Intermolecular Vibrational Coupling in Halogenated Liquids Revealed by Two-Dimensional Raman-Terahertz Spectroscopy. *J. Phys. Chem. Lett.* **10**, 4463–4468 (2019).
20. Von Hoegen, A., Mankowsky, R., Fechner, M., Först, M. & Cavalleri, A. Probing the interatomic potential of solids with strong-field nonlinear phononics. *Nature* **555**, 79–82 (2018).
21. Kozina, M. *et al.* Terahertz-driven phonon upconversion in SrTiO<sub>3</sub>. *Nat. Phys.* (2019). doi:10.1038/s41567-018-0408-1
22. Kryvohuz, M. & Mukamel, S. Multidimensional measures of response and fluctuations in stochastic dynamical systems. *Phys. Rev. A - At. Mol. Opt. Phys.* **86**, 1–12 (2012).
23. Ikeda, T., Ito, H. & Tanimura, Y. Analysis of 2D THz-Raman spectroscopy using a non-Markovian Brownian oscillator model with nonlinear system-bath interactions. *J. Chem. Phys.* **142**, (2015).
24. Sajadi, M., Wolf, M. & Kampfrath, T. Terahertz-field-induced optical birefringence in common window and substrate materials. *Opt. Express* **23**, 28985 (2015).
25. Maehrlein, S. F. *et al.* Decoding Ultrafast Polarization Responses in Lead Halide Perovskites by the Two-Dimensional Optical Kerr Effect. *Proc Natl Acad Sci USA* **19**, (2021).
26. Huber, L., Maehrlein, S. F., Wang, F., Liu, Y. & Zhu, X. Y. The ultrafast Kerr effect in anisotropic and dispersive media. *J. Chem. Phys.* **154**, (2021).
27. Grischkowsky, D., Keiding, S., van Exter, M. & Fattinger, C. Far-infrared time-domain spectroscopy with terahertz beams of dielectrics and semiconductors. *J. Opt. Soc. Am. B* **7**, 2006 (1990).
28. van Exter, M., Fattinger, C. & Grischkowsky, D. Terahertz time-domain spectroscopy of water vapor. *Opt. Lett.* **14**, 1128 (1989).
29. Spies, J. A. *et al.* Terahertz Spectroscopy of Emerging Materials. *J. Phys. Chem. C* **124**, 22335–22346 (2020).
30. Allen, S. J., Cooper, A. S., Derosa, F., Remeika, J. P. & Ulasi, S. K. Far-infrared absorption and ionic conductivity of Na, Ag, Rb, and K  $\beta$ -alumina. *Phys. Rev. B* **17**, 4031–4042 (1978).
31. Marcolongo, A. & Marzari, N. Ionic correlations and failure of Nernst-Einstein relation in solid-state electrolytes. *Phys. Rev. Mater.* **1**, 1–4 (2017).
32. Colomban, P., Mercier, R. & Lucazeau, G. Vibrational study of and conduction mechanism in  $\beta$  alumina. II. Nonstoichiometric  $\beta$  alumina. *J. Chem. Phys.* **75**, 1388–1399 (1981).
33. Colomban, P. & Lucazeau, G.  $\beta''$ - and ion-rich  $\beta$ -alumina: Comparison of vibrational spectra and conductivity parameters. *Solid State Ionics* **2**, 277–288 (1981).
34. Hao, C. H., Chase, L. L. & Mahan, G. D. Raman scattering in beta-alumina. *Phys. Rev. B* **13**, 4306–4313 (1976).
35. Chase, L. L., Hao, C. H. & Mahan, G. D. Raman scattering from sodium and silver in beta-alumina. *Solid State Commun.* **18**, 401–403 (1976).

36. Klein, P. B., Schafer, D. E. & Strom, U. Cation interstitial pair modes in the vibrational spectra of mixed  $\beta$ -aluminas. *Phys. Rev. B* **18**, 4411–4421 (1978).
37. Barker, A. S., Ditzenberger, J. A. & Remeika, J. P. Lattice vibrations and ion transport spectra in  $\beta$ -alumina. I. Infrared spectra. *Phys. Rev. B* **14**, 386–394 (1976).
38. Lucazeau, G. Infrared, Raman and neutron scattering studies of  $\beta$ - and  $\beta''$ -alumina: a static and dynamical structure analysis. *Solid State Ionics* **8**, 1–25 (1983).
39. Neugebauer, M. J. *et al.* Comparison of coherent phonon generation by electronic and ionic Raman scattering in LaAlO<sub>3</sub>. *Phys. Rev. Res.* **3**, 13126 (2021).
40. Wolf, D. On the mechanism of diffusion in sodium beta alumina. *J. Phys. Chem. Solids* **40**, 757–773 (1979).
41. Zendejas, M. A. & Thomas, J. O. Conduction mechanisms in solid electrolytes: Na<sup>+</sup> beta-alumina. *Phys. Scr.* **1990**, 235–244 (1990).
42. Walstedt, R. E., Dupree, R., Remeika, J. P. & Rodriguez, A. Na<sup>23</sup> nuclear relaxation in Na  $\beta$ -alumina: Barrier-height distributions and the diffusion process. *Phys. Rev. B* **15**, 3442–3454 (1977).
43. Iwai, Y., Kamishima, O., Kuwata, N., Kawamura, J. & Hattori, T. 109Ag NMR and relaxation mechanism in single crystal Ag  $\beta$ -alumina. *Solid State Ionics* **179**, 862–866 (2008).
44. Morgan, B. J. & Madden, P. A. Relationships between atomic diffusion mechanisms and ensemble transport coefficients in crystalline polymorphs. *Phys. Rev. Lett.* **112**, 1–5 (2014).
45. McWhan, D. B., Shapiro, S. M., Remeika, J. P. & Shirane, G. Neutron-scattering studies on beta-alumina. *J. Phys. C Solid State Phys.* **8**, L487 (1975).
46. Wakamura, K. Roles of phonon amplitude and low-energy optical phonons on superionic conduction. *Phys. Rev. B - Condens. Matter Mater. Phys.* **56**, 11593–11599 (1997).
47. Wakamura, K. Origin of the low-energy mode in superionic conductors. *Phys. Rev. B - Condens. Matter Mater. Phys.* **59**, 3560–3568 (1999).
48. Bachman, J. C. *et al.* Inorganic Solid-State Electrolytes for Lithium Batteries: Mechanisms and Properties Governing Ion Conduction. *Chem. Rev.* **116**, 140–162 (2016).
49. Krauskopf, T. *et al.* Comparing the Descriptors for Investigating the Influence of Lattice Dynamics on Ionic Transport Using the Superionic Conductor Na<sub>3</sub>PS<sub>4-x</sub>Se<sub>x</sub>. *J. Am. Chem. Soc.* **140**, 14464–14473 (2018).
50. Muy, S. *et al.* Tuning mobility and stability of lithium ion conductors based on lattice dynamics. *Energy Environ. Sci.* **11**, 850–859 (2018).